university of groningen

University Medical Center Groningen

University of Groningen

An adapted passive model of anti-MPO dependent crescentic glomerulonephritis reveals matrix dysregulation and is amenable to modulation by CXCR4 inhibition

Faycal, Chérine Abou; Oszwald, Andre; Feilen, Tobias; Contreras, Miguel de Jesus Cosenza; Schilling, Oliver; Loustau, Thomas; Steinbach, Fanny; Schachner, Helga; Langer, Brigitte; Heeringa, Peter

Published in:
Matrix biology : journal of the International Society for Matrix Biology

DOI:
10.1016/j.matbio.2022.01.001

IMPORTANT NOTE: You are advised to consult the publisher's version (publisher's PDF) if you wish to cite from it. Please check the document version below.

Document Version
Publisher's PDF, also known as Version of record

Publication date:
2022

Link to publication in University of Groningen/UMCG research database

Citation for published version (APA):
Faycal, C. A., Oszwald, A., Feilen, T., Contreras, M. D. J. C., Schilling, O., Loustau, T., Steinbach, F., Schachner, H., Langer, B., Heeringa, P., Rees, A. J., Orend, G., & Kain, R. (2022). An adapted passive model of anti-MPO dependent crescentic glomerulonephritis reveals matrix dysregulation and is amenable to modulation by CXCR4 inhibition. *Matrix biology : journal of the International Society for Matrix Biology*, *106*, 12-33. https://doi.org/10.1016/j.matbio.2022.01.001

Copyright
Other than for strictly personal use, it is not permitted to download or to forward/distribute the text or part of it without the consent of the author(s) and/or copyright holder(s), unless the work is under an open content license (like Creative Commons).

The publication may also be distributed here under the terms of Article 25fa of the Dutch Copyright Act, indicated by the “Taverne” license. More information can be found on the University of Groningen website: https://www.rug.nl/library/open-access/self-archiving-pure/taverne-amendment.

Take-down policy
If you believe that this document breaches copyright please contact us providing details, and we will remove access to the work immediately and investigate your claim.

An adapted passive model of anti-MPO dependent crescentic glomerulonephritis reveals matrix dysregulation and is amenable to modulation by CXCR4 inhibition

Chérine Abou Fayçal [a,b,c,+], Andre Oszwald [d,+], Tobias Feilen [e,g], Miguel Cosenza-Contreras [e,g], Oliver Schilling [e,h], Thomas Loustau [a,b,c], Fanny Steinbach [a,b,c], Helga Schachner [d], Brigitte Langer [d], Peter Heeringa [f], Andrew J Rees [d], Gertraud Orend [a,b,c] and Renate Kain [d]

a* - *INSERM U1109, *The Tumor Microenvironment Laboratory, Strasbourg, France*
b* - *Université Strasbourg, *Hopital Civil, Institut d'Hématologie et d'Immunologie, Strasbourg, France*
c* - *Fédération de Médecine Translationnelle de Strasbourg (FMTS), *Strasbourg, France*
d* - *Department of Pathology, *Medical University of Vienna, Vienna, Austria*
e* - *Institute of Surgical Pathology, *University Medical Center, Faculty of Medicine, University of Freiburg, Freiburg, Germany*
f* - *Department of Pathology and Medical Biology, *University Medical Center Groningen, University of Groningen, Groningen, the Netherlands*
g* - *Faculty of Biology, *University of Freiburg, Schänzlestraße 1, 79104, Freiburg, Germany*
h* - *German Cancer Consortium (DKTK) and Cancer Research Center (DKFZ), *Hugstetter Straße 55, 79106, Freiburg, Germany*
[+] These authors (CAF and AO) contributed equally to this work.

Corresponding author at: *Medical University of Vienna, Department of Pathology, Vienna, Austria*
gertraud.orend@inserm.fr, renate.kain@meduniwein.ac.at.
https://doi.org/10.1016/j.matbio.2022.01.001

Co-corresponding author at: *INSERM U1109, The Tumor Microenvironment & Tissue Matrix Laboratory, 67091 Strasbourg, France gertraud.orend@inserm.fr, renate.kain@meduniwein.ac.at.*
https://doi.org/10.1016/j.matbio.2022.01.001

Abstract

Anti-neutrophil cytoplasmic antibody (ANCA)-associated vasculitides (AAV) are severe inflammatory disorders that often involve focal necrotizing glomerulonephritis (FNGN) and consequent glomerular scarring, interstitial fibrosis, and chronic kidney disease. Robust murine models of scarring in FNGN that may help to further our understanding of deleterious processes are still lacking. Here, we present a murine model of severe FNGN based on combined administration of antibodies against the glomerular basement membrane (GBM) and myeloperoxidase (MPO), and bacterial lipopolysaccharides (LPS), that recapitulates acute injury and was adapted to investigate subsequent glomerular and interstitial scarring. Hematuria without involvement of other organs occurs consistently and rapidly, glomerular necrosis and crescent formation are evident at 12 days, and consequent glomerular and interstitial scarring at 29 days after initial treatment. Using mass-spectrometric proteome analysis, we provide a detailed overview of matrisomal and cellular changes in our model. We observed increased expression of the matrisome including collagens, fibronectin, tenascin-C, in accordance with human AAV as deduced from analysis of gene expression microarrays and tissue staining. Moreover, we observed tissue infiltration by neutrophils, macrophages, T cells and myofibroblasts upon injury. Experimental inhibition of CXCR4 using AMD3100 led to a sustained histological presence of fibrin extravasate, reduced chemokine expression and leukocyte activation, but did not markedly affect ECM composition. Altogether, we demonstrate an adapted FNGN model that enables the study of matrisomal changes both in disease and upon intervention, as exemplified via CXCR4 inhibition.

© 2022 The Authors. Published by Elsevier B.V. This is an open access article under the CC BY-NC-ND license (http://creativecommons.org/licenses/by-nc-nd/4.0/)

Introduction

Anti-neutrophil cytoplasmic antibody (ANCA) – associated vasculitides (AAV) are severe inflammatory disorders involving necrotizing inflammation of small blood vessels, often leading to irreversible tissue damage and organ failure [1]. While relatively rare with reported prevalences of 300-421 per million persons [2,3], AAV has considerable effects on premature mortality, quality of life and socio-economic cost [4–6].

AAV can manifest in any tissue but frequently involves the kidneys as focal necrotizing glomerulonephritis (FNGN), leading to irreversible renal failure [7]. Although the pathogenesis is incompletely understood, there is evidence to support the involvement of pathogenic autoantibodies (targeting myeloperoxidase, MPO, and proteinase 3, PR3), which can lead to the activation of neutrophils and their adhesion to glomerular capillary walls, resulting in focal necrosis, extravasation of plasma proteins (e.g. fibrinogen), hemorrhage, and thrombosis [8]. Furthermore, other leucocytes such as monocytes/macrophages and T cells accumulate in the periglomerular space, leading to destruction of the Bowman's capsule and subsequent proliferation of epithelial cells [7].

Over the course of weeks, injured glomeruli undergo remodeling, variably leading to the restitution of structure and function, or extensive and sometimes progressive scarring and irreversible sclerosis [7]. Common to all these processes is the degradation and synthesis of components of the extracellular matrix (ECM), a network of proteins that provides biochemical and mechanical cues and determines cellular fate [9]. Uncontrolled remodelling - potentially driven by persistent or relapsing inflammation - is considered a burden to long-term organ function due to progressive organ scarring and loss of functional tissue and regenerative capacity [10]. Understanding these changes is important for devising strategies to limit inflammation and fibrosis, and for promoting functional restitution of the kidney. Although a central role of autoimmunity to MPO has been demonstrated in mouse models [11,12], active models have many disadvantages such as the necessity to break immunological tolerance (involving administration of adjuvants), and the resulting inconsistency in disease onset. Passive models, in contrast, allow to examine the effects of pathogenic ANCA directly; however, glomerular and interstitial scarring - following acute glomerular injury in human disease – have not yet been reported in such models.

Here, we present and characterize a robust modified passive murine model of anti-MPO-dependent FNGN that progresses from acute injury with necrosis and crescents to glomerular and interstitial scarring. We show that the phenotype is comparable to renal pathology in human AAV both on morphological and molecular levels. We characterize changes in the matrisome that occur already in the acute phase. Moreover, we demonstrate the suitability of our model for pharmacological studies by applying experimental inhibition of CXCR4 using AMD3100, which reduced protein expression of leukocyte-activating chemokines. Taken together, this model may be a considerable benefit to research aimed at ameliorating progression of renal injury in AAV.

Results

Injury in human AAV results in severe matrix dysregulation

To investigate renal matrix gene expression in AAV and controls (healthy and disease), we analyzed glomerular (G) and tubulointerstitial (T) gene profiling microarray data provided by the European Renal cDNA bank (GSE104948, GSE104954) [13]. Upon analysis of defined cellular pathways annotated by the gene ontology project, we identified distinct activation of matrix-associated pathways between kidney tissue from normal human healthy living donors (LD) and AAV patients by unsupervised clustering (**Figure 1A**). On the level of individual genes, we found that quantitation of matrix-associated genes was sufficient to obtain distinct grouping of tissues from control LD and AAV patients using unsupervised clustering (**Supplementary Figure S1A**). Moreover, samples from AAV patients showed the highest degree of matrix-related pathway dysregulation scores (PDS) compared to other disease entities present in the dataset, such as diabetic nephropathy (DN), focal segmental glomerulosclerosis (FSGS), minimal change disease (MCD) and non-neoplastic tissue from tumor nephrectomy specimens (TN) (**Figure 1B**).

When filtering for matrisomal genes after differential gene expression analysis, we found 234 glomerular and 240 tubulointerstitial genes with significantly altered expression in AAV compared to LD samples (genes in the glomerular compartment: 146 up-regulated, 88 down-regulated; tubulointerstitial compartment: 114 up-regulated, 126 down-regulated, **Supplementary Tables S4, S5**). Detailed analysis revealed that several collagens (*COL1, 3, 5, 7, 11, 13, 16*), fibronectin (*FN*), tenascin-C (*TNC*), versican (*VCAN*), *emilin2* and several matrix remodeling molecules such as *MMP9, ADAMTS1, SerpinH1* and complement factors (*C1QA-C*) were significantly up-regulated in AAV tissue (adjusted $p < 0.05$) (**Figure 1C, Supplementary Figure S1B**). When comparing genes that were differentially expressed between LD and AAV, DN or FSGS, respectively, we found that AAV (vs. LD) showed the highest number of uniquely

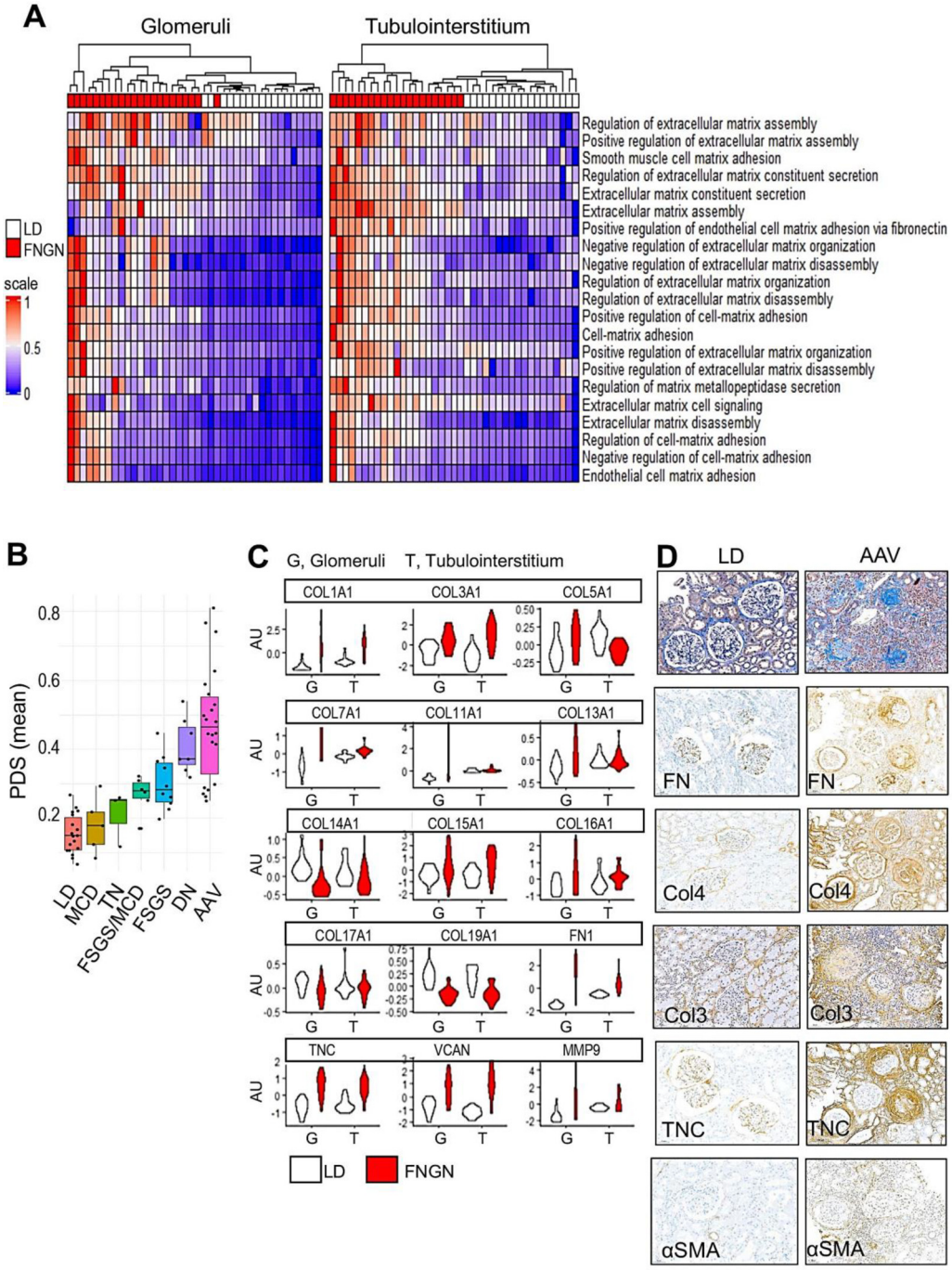

Fig. 1. AAV is associated with matrix dysregulation (A) Pathway analysis demonstrates distinct activation of ECM-associated pathways in glomerular and tubulointerstitial compartments of AAV patients upon unsupervised clustering. Data are expressed as pathway dysregulation scores (PDS) per sample. (B) AAV show high dysregulation scores of matrix-associated pathways compared to other renal diseases (LD; living donors, MCD; minimal change disease, TN; tumor nephrectomy specimen (non-neoplastic tissue), FSGS; focal segmental glomerulosclerosis). Data are expressed as mean PDS per sample. (C) Comparison of selected matrisomal gene expression between AAV (FNGN) and living donors (LD) in glomeruli (G) and tubulointerstitium (T). For specific p-values, see **Supplementary Tables S4 and S5**. (D) Renal biopsy tissues from LD and AAV patients were stained for the indicated proteins by immunohistochemistry, representative images of several cases (n = 10) are shown. Scale bar, 200 μm. Raw data was obtained from NCBI GEO (GSE104948 and GSE104954) [13].

differentially expressed genes comprising overall and matrix-associated genes (**Supplementary Figure S1C-F, Supplementary Tables S4, S5**).

We confirmed higher expression of FN, Col4, and TNC by immunohistochemistry (IHC) in sections of renal biopsies from patients with active FNGN and LD (**Figure 1D**). S100A4 and αSMA expressed by matrix-producing fibroblasts [14] were also more abundant in the AAV condition (**Figure 1D, Supplementary Figure S1B**). Thus, renal injury in AAV is accompanied by substantial changes in expression of matrisome genes [15] in both glomerular and tubulointerstitial compartments. To be able to better dissect and understand the functional implications of changes in matrisome expression along AAV evolution we developed a murine model that shares features with human AAV in clinical course and at histomorphological level.

A modified acute anti-MPO dependent murine model of FNGN mimics acute injury in human AAV

Current passive murine models of anti-MPO dependent glomerulonephritis are designed to investigate acute injury that is enhanced by co-administration of anti-glomerular basement membrane (GBM) serum or bacterial lipopolysaccharides (LPS)[12,16], but progressive injury and scarring have not yet been demonstrated. Here, we expand on this information and establish a modified AAV model by replacing the anti-MPO serum with 0.75 mg each of two monoclonal anti-MPO antibodies (clones 6D1 and 6G4, see materials) for better reproducibility and availability, administered on day 5. In order to prime glomeruli for MPO-dependent injury, we administer a sub-proteinuric dose of anti-GBM serum (100 μl, day 0), shown to be essential for injury in a murine model caused by autoimmunity to MPO [12]. **(Figure 2A)**. Following this treatment regimen, mice developed severe injury as demonstrated by assessment of macrohematuria **(Supplementary Figure S2K)**, dipstick hematuria (3+) and proteinuria (> 2+) **(Figure 2E-F)**, and approximately 20% loss of initial body weight **(Figure 2G)**. Animals were culled on day 12, when kidneys showed petechial bleeding on their surface **(Supplementary Figure S2L)**, and renal injury was confirmed by histology in 70% of glomeruli, with 10% showing fresh necrosis **(Figure 2B-C)** and 60% crescents **(Figure 2D)**. Transmission electron microscopy (TEM) revealed further ultrastructural changes such as changes in endothelial morphology, subendothelial widening and subtle electron-dense deposits **(Supplementary Figure S2S-V)**. In contrast, robust injury was not observed after single administration of either LPS (0.5 μg/g) + IgG2a/IgG2b isotype mAbs or anti-GBM serum alone (50 μl or 100 μl). Injury was also not induced by a combination of anti-GBM serum anti-MPO mAbs (day 5, or days 5 and 6), anti-GBM + IgG2a/IgG2b isotype mAbs with LPS, or anti-MPO mAbs + LPS (**Supplementary Figure S2A-J**).

AFOG staining of renal tissue, highlighting fibrin in red and ECM in blue, confirmed renal injury with extravasation of fibrin in glomeruli, indicative of endothelial damage (**Figure 2B**). This prompted us to investigate injury of the glomerular endothelium by determining the expression of markers of endothelial activation and inflammation in our AAV model mice (anti-GBM + anti-MPO + LPS) by real-time quantitative PCR (qPCR) of bulk renal RNA extracts. Accordingly, we observed significant induction of Vascular Cell Adhesion Molecule 1 (*Vcam-1*), Intercellular Adhesion Molecule 1 (*Icam-1*) and a trend towards higher E-selectin mRNA transcripts, altogether supporting endothelial cell damage in AAV model mice, but not in IgG control mice (**Figure 2H-J**).

To confirm these results and provide a broader context by gaining unbiased molecular information, we performed mass spectrometry (MS)-based proteomic analysis comparing bulk renal tissues of AAV model mice taken 12 days (12d) after disease induction with that of non-nephritic control mice injected with isotype antibodies and PBS. We observed a profound difference between conditions as demonstrated by distinct separation of samples in principal component analysis PCA (online data repository reference) and by a high number of significantly differentially abundant proteins (3070 molecules, **Supplementary Figure S2M, Supplementary Table S10**). Amongst others, we confirmed up-regulation of ICAM-1 and VCAM-1 at the protein level (**Figure 2K**). Moreover, several protein signatures comprising 79 genes indicating immune response activation and other distinct inflammatory pathways were up-regulated in AAV model mice compared to control mice, providing a detailed characterization of inflammation in our AAV model kidney tissue (**Figure 2K, Supplementary Figure S2N-R**).

Next, we performed a detailed comparison of the available human gene expression and our murine proteomic datasets. Murine protein abundance showed a highly significant ($p < 2.2^{-16}$) moderate correlation to the respective human glomerular ($\rho = 0.41$) and tubulointerstitial ($\rho = 0.42$) transcript abundance (Spearman's rank correlation test). On the level of individual genes, we found that 1091 (35.54%) of proteins with significant differential abundance (adj. $p < 0.05$) in our proteomic analysis had human homologues with concordant differential transcript expression in AAV patients, representing 13.6% and 12.4% of all human glomerular or tubulointerstitial genes, respectively, with significant differential expression in AAV patients (**Supplementary Tables S7-S9**). Moreover, 316 (10.29%, glomerular) or 575 (18.73%, tubulointerstitial) of proteins with significant differential abundance in our proteomic analysis had human homologues with concordant

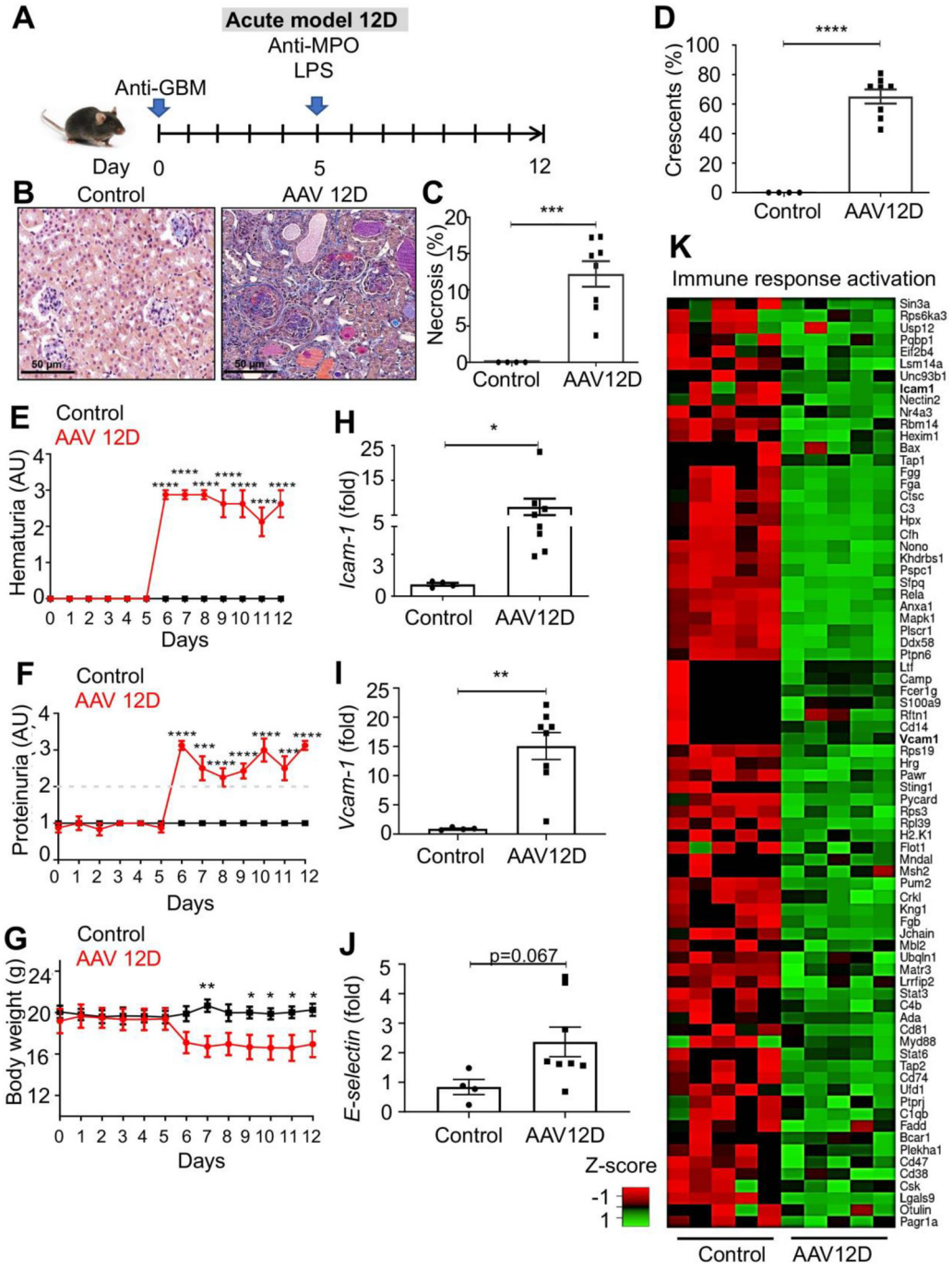

Fig. 2. Histopathological and clinical characterization of acute injury in an adapted murine AAV model (A) Schematic representation of the treatment protocol leading to acute AAV injury examined at day 12d. Controls: female C57Bl6J mice were injected with PBS by (i.v., tail vein) on day 0 and received 0.75 mg of each IgG2a and IgG2b isotype control antibodies (i.p.) followed by PBS injection (i.p.) one hour later at day 5, N = 4. AAV model mice: female C57Bl6J mice received 100 µl anti-GBM serum (i.v.) on day 0, followed by injection of two monoclonal anti-MPO antibodies (i.p.) and LPS (0.5 µg/g, i.p.) one hour later on day 5, N = 8. (B) Representative images (N = 4 for control, N = 8 for AAV) of AFOG-stained tissue, scale bar 50 µm. (C, D) Quantitation of glomeruli with necrosis (C) or crescents (D) in percent of all glomeruli. (E, F) Dipstick urine measurement of hematuria (E) and proteinuria (F). (G) Body weight measurements. (H-J) qPCR analysis showing relative gene expression of endothelial cell markers differentially regulated during inflammation: *Icam-1* (H), *Vcam-1* (I) and *E-selectin* (J). Mean +/- SEM, each mouse represents a data point. N = 4, control, N = 8, AAV. T-tests or Mann-Whitney U-test, * = $p < 0.05$, ** = $p < 0.01$, *** = $p < 0.001$, **** = $p < 0.0001$. (K) Proteomic analysis reveals proteins enriched in pathway analysis under the Gene Ontology term “Immune response activation” (enrichment $p = 4.75^{-04}$. Data are presented as centered and scaled abundance values, n = 5 mice per group.

differential transcript expression that was unique in AAV patients (compared to DN or FSGS), representing 14.88% (glomerular) or 10.08% (tubulointerstitial) of genes with significant differential transcript expression unique for AAV patients.

Taken together, these results show that our adapted protocol employing anti-GBM, two monoclonal anti-MPO antibodies and LPS together is sufficient to induce severe FNGN with crescent formation in mice, resembling human AAV, whereas injury was not observed or only minor in mice that did not receive all three components.

The acute phase of anti-MPO antibody-induced FNGN presents with inflammatory conditions and increased immune cell infiltrate

As indicated by the proteomics analysis, we further investigated the activation of the immune response and characterized the leukocyte infiltrate by immunostaining of tissue sections and qPCR analysis of inflammatory cytokines in kidney tissue from AAV model mice 12d after disease induction. By IIF and IHC, we found an increase of CD45+ leukocytes within both the glomeruli and tubulointerstitium of kidneys from our AAV model, in contrast to control conditions **(Figure 3A-B, Supplementary Figure S3A)**. Using specific antibodies, we found an increase of neutrophils (MPO, NE), macrophages (CD68+), T-cells (CD3+) and regulatory T-cells (FoxP3+) in glomeruli and tubulointerstitium of AAV model kidneys (**Figure 3C-E, Supplementary Figure S3B-G)**.

By qPCR and tissue staining with specific antibodies, we observed increased expression of CXCR4 mRNA and protein, whose involvement in renal disease has been previously implied [17,18]. Interestingly, we found CXCR4 highly expressed in cells forming the crescents in the Bowman's capsule, reminiscent of CXCR4 expression in podocytes as described [17] (**Figure 3F-G**). Using qPCR, we determined that expression of CXCL12 (a CXCR4 ligand), CXCL1 and CXCL2 (chemoattractants for several immune subtypes, including neutrophils [19]) was elevated in AAV compared to control conditions (**Figure 3H-J**). In addition, we found increased mRNA expression of pro-inflammatory cytokines *TNF, IL1β* and *IL6* in renal tissue of AAV model mice **(Figure 3K-M)**. These data are consistent with the MS-based proteomics findings, which indicated positive regulation of cytokine production **(Supplementary Figure S2N)** associated with production of TNF **(Supplementary Figure S2O)** and an induction of responses to IL1 **(Supplementary Figure S2P)** and IL6 **(Supplementary Figure S2Q)**.

We correlated these findings from our murine model to human disease by interrogating available gene expression microarray datasets (ERCB; GSE104948 and GSE104954), which showed higher expression of *CXCL1, CXCL2, TNFα, IL1β, IL6* and CXCR4 in renal tissues from AAV patients than in those of living donors (LD) (**Supplementary Table S6**). Thus, our murine acute AAV model phenocopies important immunological features of human AAV.

Extracellular matrix molecules are up-regulated in the acute phase of anti-MPO antibody-induced FNGN

Deposition of extracellular matrix molecules such as collagens is a known consequence of renal injury in AAV that leads to glomerular and interstitial scarring [1], as confirmed by the differential gene expression analysis using data provided by the European Renal cDNA bank (GSE104948, GSE104954) [13]. The unbiased MS-based proteomic analysis of renal tissue from the acute phase of our anti-MPO-dependent FNGN model revealed significant differential abundance of 40 matrisome proteins, including structural molecules such as several collagens (Col1a1, Col3a1, Col1a2, Col18a1), Emilin1, FN, Fibulin-1, Fibulin-5, Periostin, Vitronectin, Lumican, TNC, and ECM regulatory molecules such as serpins, further defining changes in the matrisome of AAV model mice **(Figure 4A).**

Using qPCR, IIF and IHC on renal tissue sections from AAV model mice, we confirmed that both mRNA and protein expression of collagens *Col1a1* and *Col3a1, Fn* and *Tnc* was higher in the FNGN model than in control tissue, indicating transcriptional regulation of these molecules (**Figure 4B-I**). Fibroblastic cells are known to produce matrix in kidney disease, involving TGFβ signaling [1]. MS-based proteomic analysis reflected a TGFβ response signature of 22 genes up-regulated in FNGN compared to control kidney tissue (**Supplementary Figure S2R**). By tissue staining and qPCR, we confirmed higher αSMA and *Tgfb* expression in FNGN than control tissue, suggesting increased abundance of pro-fibrotic fibroblasts (**Figure 4J-L**).

Importantly, analysis of the available ERCB datasets (GSE104948, 104954) showed concordant upregulation of *FN, Col1A1, Col3A1, TGFβ* and *TNC* in AAV patient samples compared to living donors (**Supplementary Table S4 and S5**). Overall, these data show that in the acute phase of our murine anti-MPO antibody model of FNGN, matrisomal changes occur, including expression and deposition of extracellular matrix proteins, which recapitulates the findings in patients with FNGN in the context of AAV.

Development of an adopted murine anti-MPO dependent late-stage FNGN model that emulates features of chronic human renal AAV

Chronic injury in AAV is characterized by onset of new lesions in the context of manifest scarring injury. Despite a number of previously established models

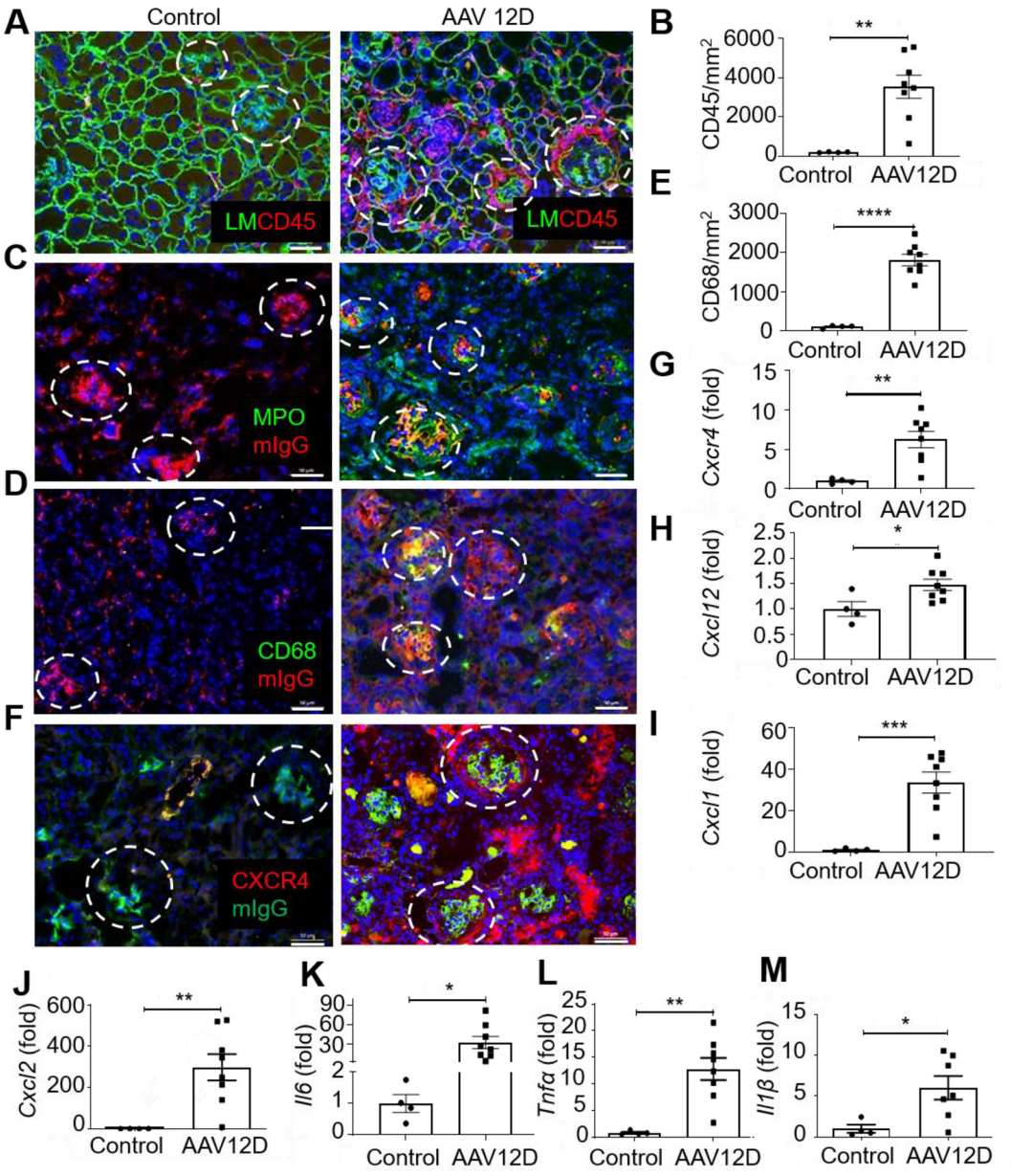

Fig. 3. Characterization of immune cell infiltrates in kidney tissue of acute FNGN model (A, C, D, F) Renal tissue from control (N = 4) and FNGN (N = 8) mice was stained with the indicated antibodies by indirect immune-fluorescence, DAPI was used as nuclear marker (representative images shown, scale bar, 50 μm). Glomeruli are encircled. (B, E) Quantitation of leukocytes (cells per mm^2) on tissue sections labelled by IHC with antibodies to CD45 (B) or CD68 (E). (G-M) qPCR analysis showing relative gene expression levels of *Cxcr4* and *Cxcl12* (G, H), neutrophil-related chemokines (I, J) and inflammatory cytokines (K-M). N = 4 control, 8 FNGN points represent individual mice. Horizontal lines and bars correspond to mean +/- SEM; normality test was performed and the results were analyzed using T-tests if the normality test was fulfilled, otherwise by Mann-Whitney U-test, * $p < 0.05$, ** $p < 0.01$, *** $p < 0.001$, **** $p < 0.0001$.

of AAV, it remains challenging to model the phenotype of chronic injury [20]. We evaluated the feasibility of our protocol to emulate chronic scarring renal disease by observing mice for increasing time periods (after 12, 19, 24 and 29d) upon induction of injury with anti-GBM/anti-MPO/LPS (as described for the acute model) (**Figure 2A, 5A**). Dipstick measurements showed that severe hematuria was sustained at high levels (3+) for approximately 10 days before a slight decrease, and continued to be strong (2+) until the end of observation at day 29 **(Figure 5F)**. Moreover, proteinuria remained at high levels (3+) until day 29 **(Figure 5G)**. Finally, mice did not recover body

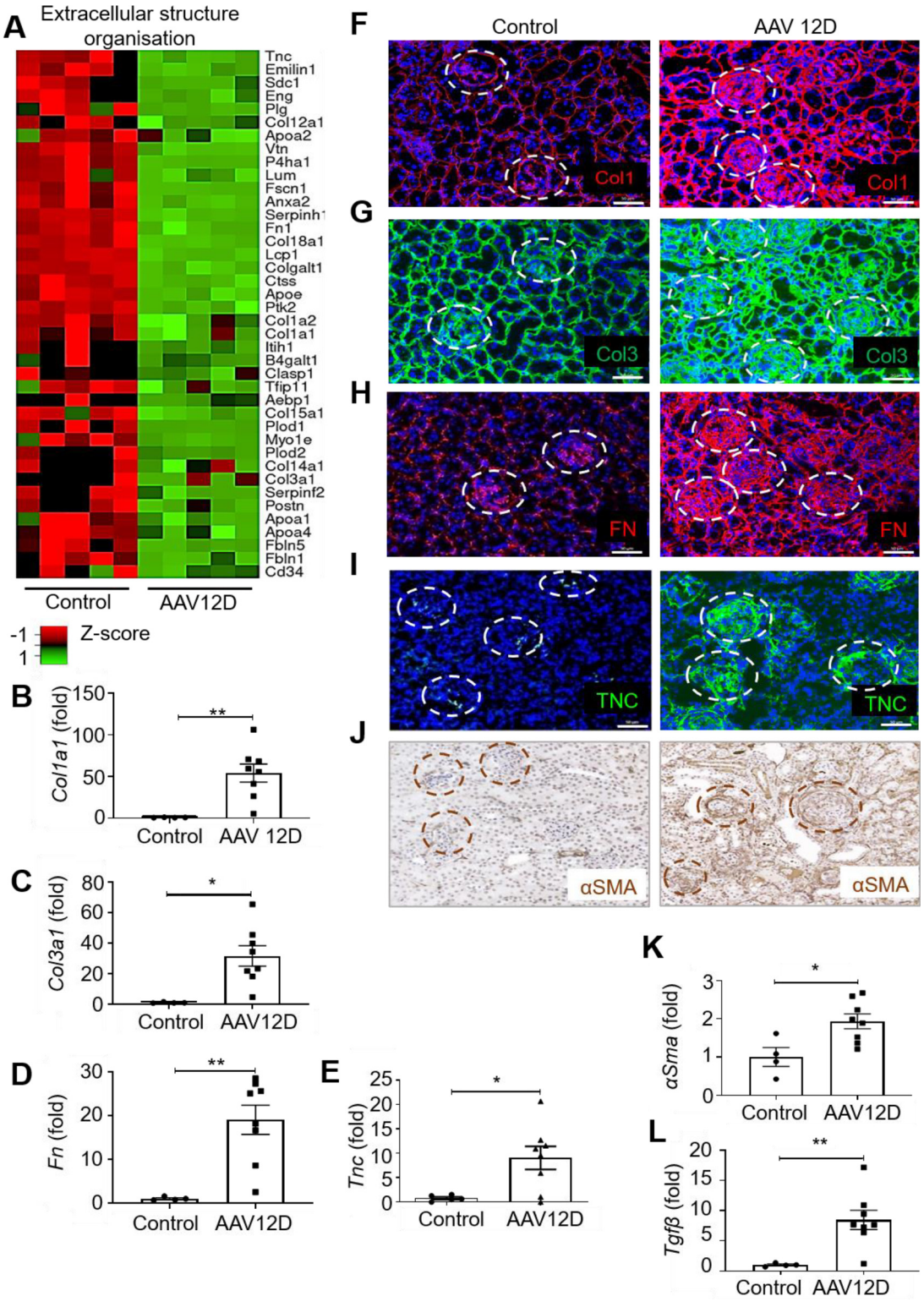

Fig. 4. Characterization of extracellular matrix deposition and fibroblast markers in the acute AAV model by MS, IHC, IIF and qPCR. (A) Heatmap showing significant differential abundance of proteins enriched for Gene Ontology annotation "extracellular structure organization" ($p = 8.59^{-07}$) between AAV model mice culled on day 12 and control mice without injury (adjusted $p<0.05$, N = 5 mice per group, data are presented as centered and scaled abundance values). (B-E, K-L) qPCR analysis of the indicated molecules, points represent individual mice, mean +/- SEM. Normality test was used and the results were analyzed using T-tests if the normality test was fulfilled otherwise by Mann-Whitney U-test, * $p < 0.05$, ** $p < 0.01$. (F-J) Representative images of renal tissues from control (N = 4) and AAV (N = 8) mice investigated by IIF (F-I) and IHC (J) with the indicated antibodies; scale bar = 50 μm. Glomeruli are encircled.

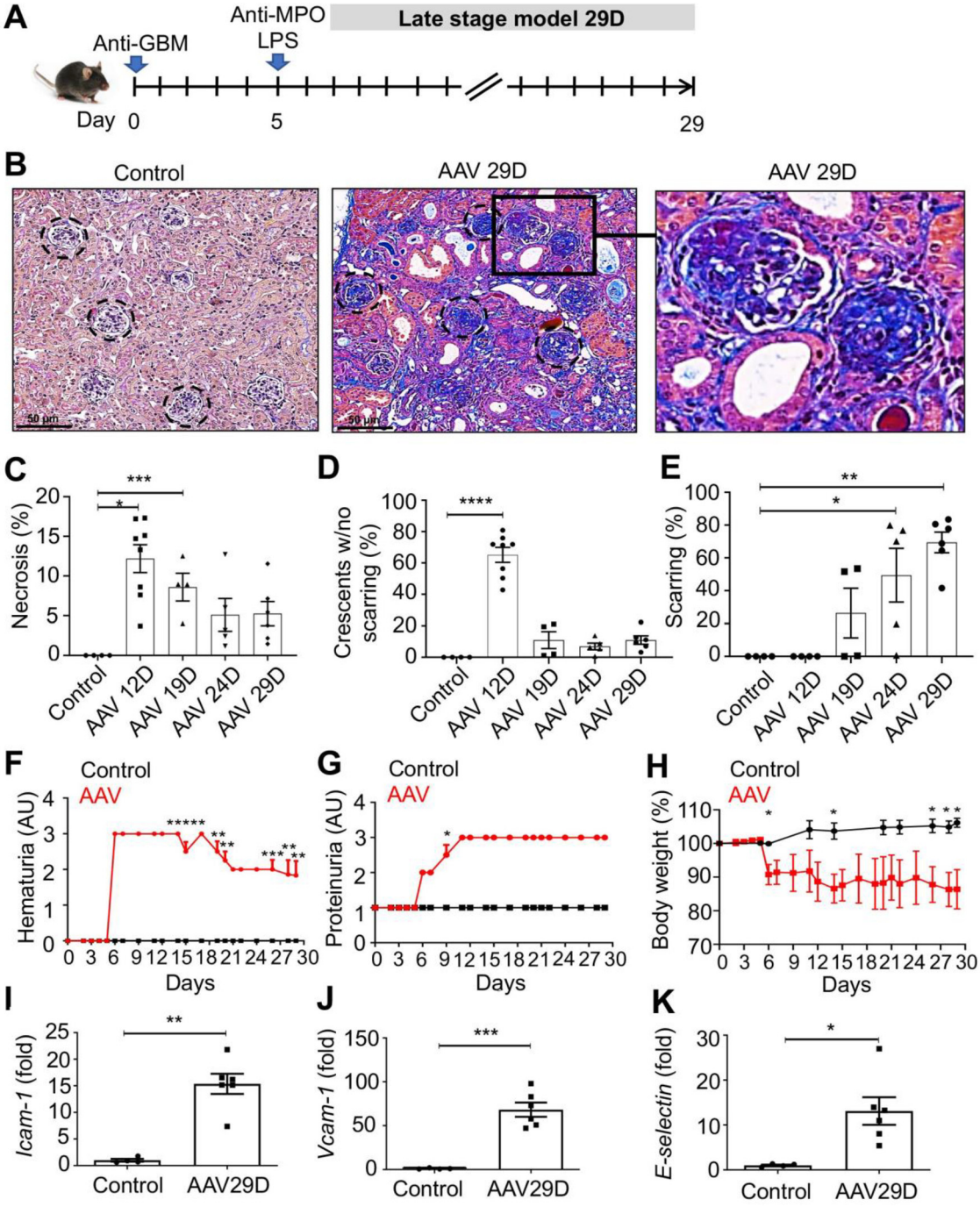

Fig. 5. Histopathological and clinical characterization of late-stage injury in the modified murine AAV model (A) Schematic representation of the treatment protocol with collection of murine kidneys at day 19, 24 and 29. Control mice received injection of PBS by tail vein (i.v.) at day 0, followed by 0.75 mg each of murine IgG2a and IgG2b isotype antibodies (i.p.) at day 5, and PBS (i.p.) one hour later (N = 4). For model AAV, mice were injected with anti-GBM serum (i.v.) on day 0, followed by 2 monoclonal anti-MPO antibodies (i.p) on day 5, and 5 μg/g LPS (i.p.) one hour later. Kidneys were collected on days 12 (N = 8), 19 (N = 4), 24 (N = 5) and 29 (N = 6). (B) Representative images from AFOG stained kidney sections of control and AAV model mice after 29d. Black circles highlight the glomeruli. Higher magnification on the far right illustrating extensive scarring of glomeruli (blue). (C-E) Quantitation of glomerular injury with necrosis (C), crescents (D) and scarring (E) in percent of all glomeruli. (F, G) Dipstick urine measurement of hematuria (F) and proteinuria (G) and body weight measurement (H) of 29d control and AAV model mice. (I-K) qPCR analysis of inflammatory endothelial cell markers as indicated. Mean +/- SEM, one dot per mouse. Normality test was performed and the results were analyzed using T-test if the normality test was fulfilled, otherwise by Mann-Whitney U-test, * $p < 0.05$, ** $p < 0.01$, *** $p < 0.001$, **** $p < 0.0001$, ***** $p < 0.00001$.

weight loss within 29d of observation (**Figure 5H).** By AFOG staining, we determined the relative abundance of healthy and diseased glomeruli (i.e. presenting necrosis, crescents and scarring) following disease induction (**Figure 5B-E, Supplementary Figure S4A**).

Necrotizing injury without scarring peaked at 12d (with over 60% of glomeruli affected) followed by a decline at the other time points to less than 10% of affected glomeruli. In contrast, the number of glomeruli with scarring increased at 19, 24 and 29d and was highest at 29d (70%). Sirius red stain revealed substantial glomerular and tubulointerstitial scarring, attaining highest levels at 29d post injury (**Supplementary Figure S4C**). Accordingly, the 29d time point was chosen for further detailed analysis. Importantly, at this time point few glomeruli exhibited only necrosis (5%) or crescents without scarring (10%), indicating that new lesions were still generated around 29d after disease induction. Using TEM, we found electron dense deposits in the mesangium, subendothelial and subepithelial space **(Supplementary Figure S2W-Z)**. Via qPCR, we identified increased expression of *Vcam-1, Icam-1* and *E-selectin*, demonstrating the persistence of endothelial activation **(Figure 5I-K).**

Tubular injury, atrophy and tubulointerstitial fibrosis are common in biopsies of patients with AAV. Similarly, in our murine model we observed extensive tubular injury, atrophy, incipient fibrosis, and plenty of tubular casts as a sign of reduced diuresis in the medullary tubulointerstitial compartment (**Supplementary Figure S4D-E**).

Taken together, our murine anti-MPO model of FNGN shows progression of acute injury into extensive renal scarring, with fresh lesions occurring even at a later time point. Thus, this model recapitulates several important clinicopathological features of chronic injury observed after FNGN in AAV patients.

Leukocyte infiltrate is sustained in the murine late-stage AAV model

At 29d post disease induction, we observed high numbers of infiltrating CD45+ leukocytes, similar to the early time point (**Figure 6A-B, Supplementary Figure S5A**). Moreover, we found similarly high numbers of infiltrating CD68+ macrophages, but 4-times more CD3+ T cells and 2-times more FoxP3+ Treg at 29d than at 12d, further supporting evolution of injury (**Figure 6C-F, Supplementary Figure S5B-E**). Via qPCR, we determined *IL6* and *TNFα* to be 2-times higher at 29d than at 12d, while *CXCL1, CXCL2, IL1β* and *CXCR4* (the latter also demonstrating expression via IF in both glomeruli and interstitium) remained at similar levels at 29d and 12d (**Figure 6G-M**). In contrast to 12d, *Cxcl12* levels were only slightly elevated at 29d ($p = 0.11$) (**Supplementary Figure S5F**).

Overall, we conclude that scarring injury in our AAV model comprises a sustained, complex infiltration of leukocytes in renal tissue – an important feature of the chronic disease in human AAV patients.

Extracellular matrix molecules are up-regulated in the late-stage murine anti-MPO antibody model of FNGN

One of the hallmarks of chronic renal disease in general is the accumulation of matrix, culminating in renal fibrosis [21]. We determined an accumulation of collagens in the kidney at 29d using sirius red staining and quantitative analysis of stained renal cortex area **(Figure 7A-B)**. Concordantly, we found significantly increased protein and mRNA expression of Col1 (COL1A1), Col3 (COL3A1), FN and TNC in kidneys of late-stage anti-MPO model mice at 29d (**Figure 7C-H**). Of note, *Tnc* mRNA expression was 2-times higher at 29d than at 12d post injury, and co-expressed with collagens in tissue sections (**Figure 4H, 7J**), suggesting a particular role of TNC in scarring.

We found a 20-fold increase of *Vim* mRNA expression in renal tissue of AAV model mice compared to control mice ($p = 0.06$), suggesting a higher abundance of fibroblasts, potentially greater at 29d than at 12d (**Figure 7L**). We found a non-significant increase in *Tgfβ* expression compared to control mice ($p = 0.059$) at similar levels as at 12d, suggesting a potential continuous role of TGFβ signalling during disease progression. In contrast to the acute stage, at 29d *acta2* mRNA was similar between control and injured mice (**Supplementary Figure S6A-B**).

CXCR4 inhibition reduces the activation of immune cells in the murine AAV model

It was previously shown that CXCR4 plays a central role in a monogenic murine model of crescentic glomerulonephritis caused by *VHL gene* deficiency in intrinsic glomerular cells [17]. Our results confirmed elevated CXCR4 expression at early and late time points after injury in our modified murine AAV model and we therefore exploited the potential modulatory role of CXCR4 by treating our mice with an FDA-approved inhibitor of CXCR4 [22] (AMD3100, abbreviated AMD) over the course of our acute AAV model protocol (12d) (**Figure 8A)**. AMD treatment did not affect dipstick hematuria, proteinuria or body weight loss **(Supplementary Figure S7A-C)** or the overall abundance of injured glomeruli (necrosis, crescents) **(Supplementary Figure S7D-F)**. However, in AFOG staining (highlighting fibrin in red and ECM in blue), we found that glomeruli exhibiting both crescents and fibrinoid necrosis together were

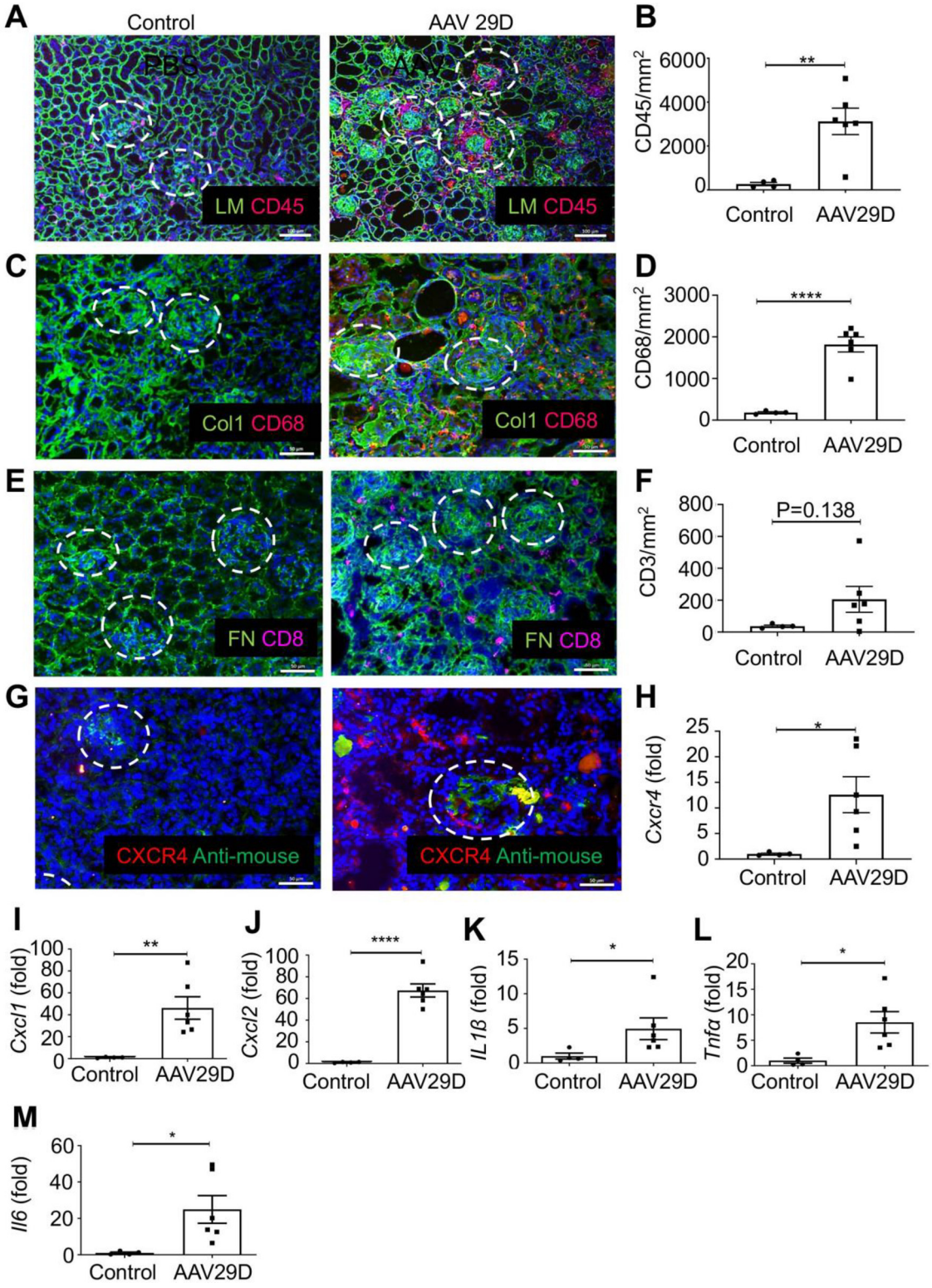

Fig. 6. Characterization of the immune cell infiltrate in the late-stage AAV model (A, C, E, G) Representative immunofluorescence images from renal tissues of control (N = 4) and AAV (N = 6) mice with the indicated antibodies, scale bar, 50 μm. Glomeruli are encircled. (B, D, F) Quantitation of immune cells characterized by IHC with antibodies indicated, expressed as cells per mm^2. (H-M) qPCR results for the indicated molecules using bulk RNA from renal tissue of AAV model mice (N = 6) and controls (N = 4). Mean +/- SEM with individual mice as data points. Normality test was performed and the results were analyzed using T-tests if the normality test was fulfilled otherwise Mann-Whitney U-test was used, * $p < 0.05$, ** $p < 0.01$, ****** $p < 0.0001$.

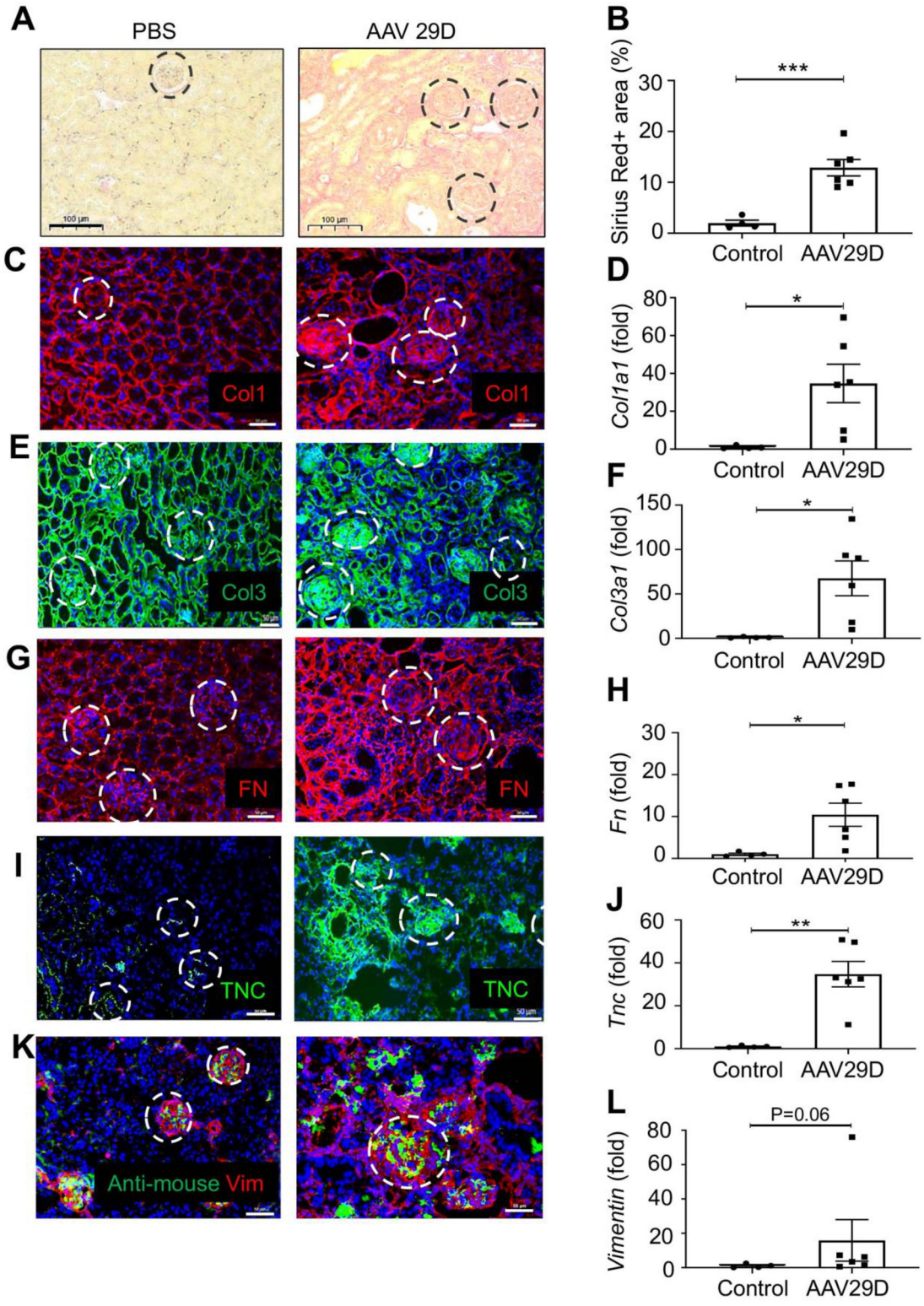

Fig. 7. Characterization of extracellular matrix deposition and fibroblast markers in the late-stage AAV model (A) Staining and (B) quantitation of collagen fibers on renal tissue sections from control (N = 4) and AAV (N = 6) mice with Sirius red, expressed as % of total area. (C, E, G, I, K) Representative images (control (N = 4) and AAV (N = 6) mice) from IIF stained renal tissue with the indicated antibodies, scale bar, 50 µm. Glomeruli are encircled. (B, D, F, H, J, L) qPCR results for the indicated genes in control (N = 4) and AAV (N = 6) mice, mean +/- SEM with individual mice as data points. Normality test was performed and the results were analyzed using T-tests if the normality test was fulfilled, otherwise Mann-Whitney U-test was used. * $p < 0.05$, ** $p < 0.01$, *** $p < 0.001$.

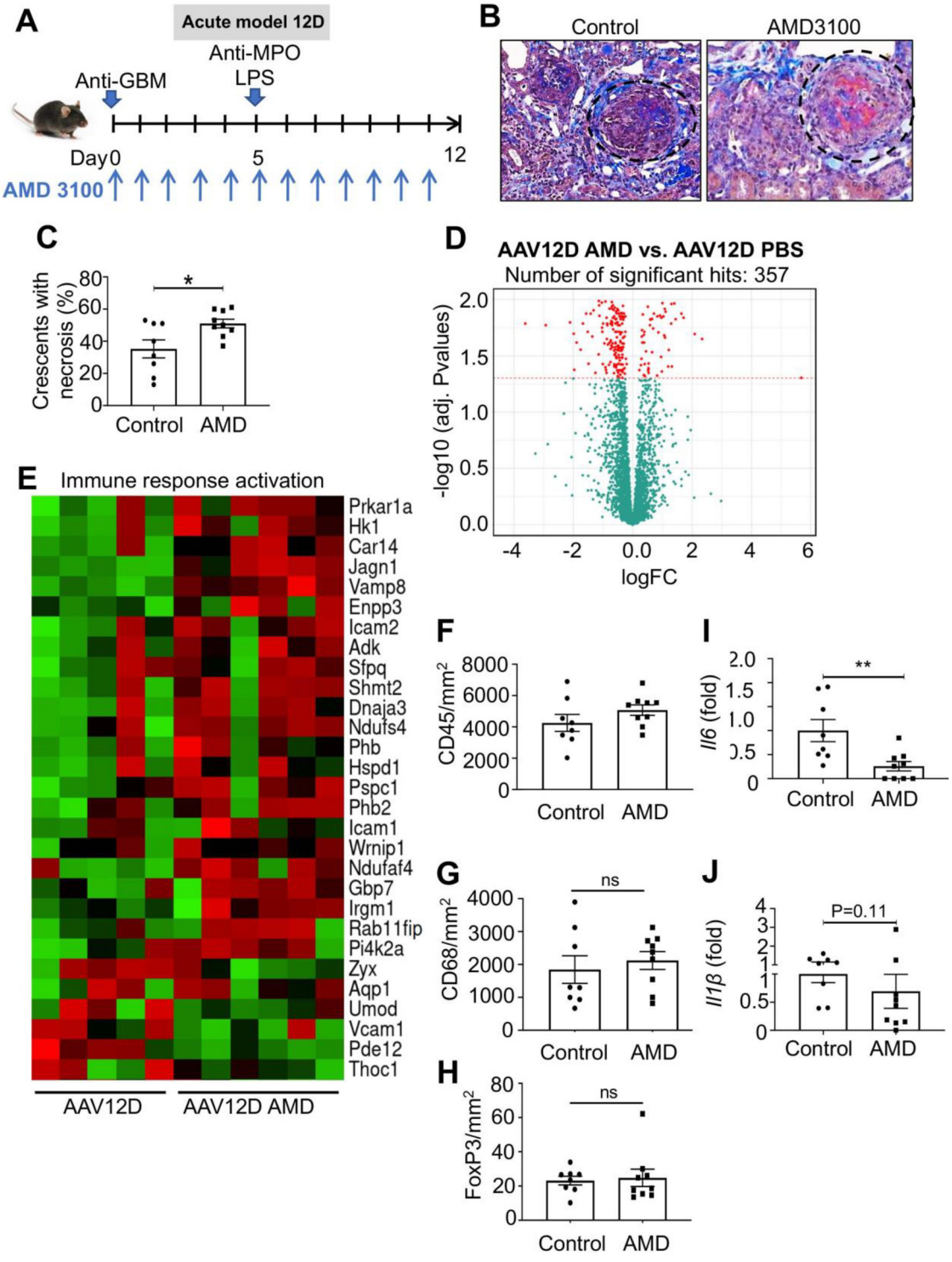

Fig. 8. Impact of CXCR4 inhibition on acute kidney injury in the 12d AAV model (A) Schematic representation of the injection protocol. AAV model mice were treated with AMD 3100 from day 0 onwards. Mice received anti-GBM serum (i.v.) on day 0, two monoclonal anti-MPO antibodies (0.75 mg each, i.p.) on day 5 followed by LPS (5 μg/g) one hour later. AMD was administered daily (0.2 mg) (N = 9), vehicle control was PBS (N = 8). Kidney tissue was collected at day 12 after treatment. (B) Representative images of AFOG stain. (C) Quantitation of injured glomeruli presenting with crescents and residual fibrinoid necrosis as percent of total glomeruli. (D) Proteomic analysis reveals differentially abundant proteins in control (N = 5) and AMD mice (N = 6), displayed as volcano plot. Red dots represent genes with significant differential abundance ($p < 0.05$) (E). Heatmap showing differentially abundant proteins with Gene Ontology

more frequent, suggesting that AMD may either prolong the presence of fibrin extravasates or results in prolonged endothelial injury resulting in fibrin extravasation **(Figure 8B-C)**.

To clarify this, we used MS-based proteomics and determined 357 proteins in kidneys of AAV model mice treated with AMD with significant ($p<0.05$) differential abundance compared to AAV model mice treated with control PBS injections **(Figure 8D, Supplementary Table S11)**. Notably, AMD-treated mice showed reduced abundance of proteins involved in leukocyte activation **(Figure 8E).** Via qPCR, we could confirm a significant reduction of *Il6* mRNA transcripts, but not of *Il1b* ($p = 0.11$), CXCL1 or CXCL2, after AMD treatment (**Figure 8I-J, Supplementary Figure S7G-H).** We found no difference in the abundance of leukocytes (CD45+), macrophages (CD68+, CD206+), T cells (CD3+), regulatory T cells (Foxp3+) or neutrophils (MPO+) in the cellular infiltrate after AMD treatment **(Figure 8F-H, Supplementary Figure 7I),** suggesting that activation, but not abundance, of immune cells was affected by AMD. We identified no unequivocal effect of AMD on abundance of matrisome proteins, and found individual proteins with higher (Col1a2, Col6a1) or lower (Col3a1) abundance after AMD treatment (**Supplementary Figure S7L**).

Taken together, these results suggest that immune cell activation and injury in our anti-MPO antibody model of AAV are sensitive to inhibition of CXCR4, which may prove a viable target for modifying renal injury. Moreover, it exemplifies that our model is suitable for pre-clinical studies of pharmacological intervention at early and late stages of renal injury AAV.

Discussion

To date, several animal models of AAV to study the pathogenesis of the disease have been developed and investigated, in particular loss of tolerance to self-antigens and the roles of specific components of the immune system [20]. Such models revealed a role of complement factors in glomerular injury of AAV and instigated a phase 3 clinical trial using a selective C5aR inhibitor (NCT02994927) [23]. However, we are still lacking a robust murine model that emulates the progression of acute necrotizing glomerular injury to glomerular and tubulointerstitial scarring, which involves extensive deposition of extracellular matrix [24]. In particular, a model of chronic or relapsing AAV, which is a major determinant of end stage renal disease in humans [1], could be valuable in evaluating novel targeting strategies [25].

In this study, we established and characterized a modified murine AAV model that demonstrates robust anti-MPO antibody-dependent, immune-mediated injury in form of fibrinoid necrosis and glomerular crescents after 12d, and extensive scarring of glomeruli and tubulointerstitium after 29d with persistent generation of acute lesions. In addition, our model reflects pertinent clinical features of AAV, notably severe hematuria, proteinuria and weight loss (**Figure 9**).

To achieve this, we applied consecutive injections of sheep serum raised against glomerular basement membrane (GBM) epitopes, followed by injection of two monoclonal murine antibodies against MPO in combination with LPS. The rationale behind this protocol is that anti-GBM serum recruits leukocytes (especially neutrophils) to the glomerulus, where a deposition of MPO occurs [26], murine monoclonal anti-MPO antibodies then target persistent inflammation to the glomerular basement membrane. LPS is a common trigger of immunological responses, for instance to bacterial infections, which are often observed prior to onset of AAV in humans [27]. In our model, injury is dependent on the combined application of all three components, since each component alone or in a pairwise combination failed to induce robust injury.

Our approach has several practical advantages over other models of AAV. Passive immunization is faster than active and does not require the use of adjuvants such as Complete Freund's Adjuvant (CFA), which may cause severe pain and distress to the animal. Moreover, the immunological response of animals to active immunization is highly variable between experiments or laboratory environments, whereas passive administration has a reproducible time of onset. Lastly, the generation of murine anti-MPO serum, employed previously, requires active immunization of MPO deficient (-/-) mice. Therefore, using monoclonal murine antibodies greatly increases availability and batch-to-batch reproducibility of reagents and reduces the number of experimental mice.

The modifications we applied to published passive transfer models of AAV resulted in increased severity and a phenotype that exhibits substantial glomerular scarring (in up to 70% of glomeruli), previously not reported in models of AAV. Huugen et al. (2005) have shown that combined injection of a polyclonal anti-MPO antibody (100 μg/g) together with LPS (0.5 μg/g) induced injury with crescents in 20% of glomeruli after 6 days [16]. In comparison, the

annotation for immune response activation (enrichment $p = 0.07$). Data are presented as centered and scaled abundance values. Quantitation of (F) CD45+ cells (G) CD68+ cells and FoxP3+ cells (H) upon IHC staining expressed as cells per mm^2. (I, J) Gene expression results (qPCR) for the indicated molecules in control (**N = 9**) and AMD treated conditions (**N = 9**), mean +/- SEM with individual mice as data points. Normality test was performed and the results were analyzed using T-tests if the normality test was fulfilled otherwise Mann-Whitney U-test was used, ** $p < 0.01$.

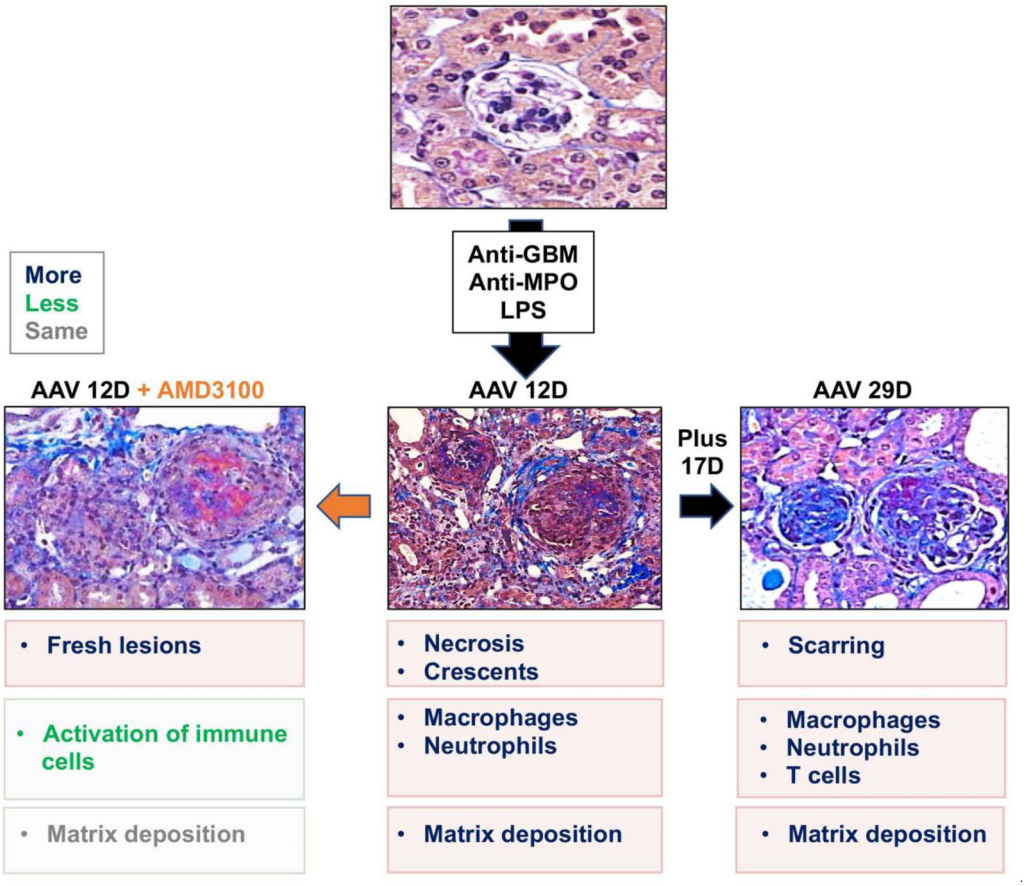

Fig. 9. Summary of a modified acute and late-stage AAV model In the acute AAV model (12d) we observed necrosis and crescent formation with neutrophils and macrophages infiltrating the glomeruli and tubulointerstitium. Matrix molecules were highly expressed. In the late-stage AAV model (29d), glomerular scarring was observed in addition to necrosis and crescents. Macrophages and lymphocytes infiltrated the kidney tissue in high numbers and deposition of matrix molecules increased. Targeting AAV model mice with the CXCR4 inhibitor (AMD3100, daily administration starting at day 0) increased the percentage of crescents with residual fibrinoid necrosis. AMD3100 did not affect quantity of immune cell infiltrate; however, unbiased proteomic analysis suggested reduced leukocyte activation.

frequency of crescentic injury in our model was 3-times greater. Importantly, by unbiased MS-based proteomics, we report extensive changes in matrisome expression (including but not limited to collagens, FN and TNC) that occur already in acute injury.

As a characteristic feature of AAV, we observed massive leukocyte infiltration comprising neutrophils, macrophages, T-cells (including Tregs), with higher abundance of macrophages and T-cells at later compared to earlier time points. Moreover, using both unbiased mass spectrometry (MS)-based proteomics, immunofluorescence and qPCR, we demonstrated and confirmed induction of pro-inflammatory cytokines.

Using TEM, we found further evidence of glomerular injury in renal cortex tissue from representative mice, which demonstrates at day 12 glomerular endothelial activation and confirmed segmental necrosis with fibrin extravasation and crescent formation, however only occasional segmental subendothelial widening with deposition of mainly electron-lucent material. In addition, at day 29, we observed segmental sclerosis with small segmental mesangial and occasional subepithelial and subendothelial deposits. These changes affected a proportion of the glomeruli only, similar to those seen in approximately 18% of patients with FNGN in AAV and that are associated with proteinuria and worse prognosis [28].

In order to compare molecular features of human and murine disease, we interrogated available gene expression datasets (European Renal cDNA bank, GEO accession GSE104948 and GSE104954) [13] and determined substantial deregulation of ECM-associated pathways and overexpression of matrisome components in glomeruli and tubulointerstitium from AAV patients compared to both healthy living donor, but also other renal diseases. Importantly, we found concordance between human AAV

and our mouse model regarding both ECM molecules (collagens 1 and 3, FN and TNC) and inflammatory cytokines such as CXCL1, CXCL2, CXCL12, IL1β and IL6, which are relevant in human AAV [29].

TNC can act as a danger associated molecular pattern (DAMP) [30] and was highly induced both in human AAV patients as well as in our AAV model. Previously, TNC was found to be significantly increased in serum of AAV patients (145 ng/ml) in comparison to healthy subjects (48 mg/ml), suggesting that TNC could qualify as a biomarker of AAV [31]. Together with respective human studies, our model has the potential to further biomarker research for human disease, for instance relating to disease activity or estimating the latest timepoints up to which anti-inflammatory or anti-fibrotic therapy are likely to have a beneficial effect.

Our observation of substantial matrisomal alterations in the absence of fibrosis at the acute phase (12 days post treatment) is important, novel and not expected. Thus, our results suggest that dynamics in the matrisome precede fibrosis, the latter becoming prominent in the late stage of the model at 29 days after injury.

We found moderate correlation of our proteomic analysis with human glomerular and tubulointerstitial gene profiling datasets. Detailed comparison demonstrated that a substantial proportion (35.54%) of murine proteins differentially expressed in our model correspond to differentially expressed transcripts in human AAV, approximately one third of which were uniquely dysregulated in AAV. Although we consider this a substantial overlap, two plausible reasons for obtaining less than identical concordance are the non-linear relation of transcripts and protein, and differences between human and murine organisms. The latter are especially important to consider in evaluating limitations in resemblance to human disease. In summary, our murine model recapitulates several important features of human AAV at the clinical, morphological, cellular and molecular level.

AAV is a systemic autoimmune disease that often can affect other highly vascularized organs such as the lung or skin, peripheral nervous system or the heart. Upon histopathological analysis, we observed no histomorphological changes consistent with vasculitis such as vascular necrosis, thrombosis, inflammation or haemorrhage or scarring in any other mouse organs investigated (lung, heart, liver, intestine, skin). Mice that received anti-GBM serum, anti-MPO antibodies and LPS showed increased splenic germinal centers at 12d and 29d (data not shown), likely reflecting the systemic immune response provoked by administration of LPS and foreign protein. Both experimental and control mice receiving only PBS and isotype IgG showed inconsistently very discrete foci of inflammatory infiltrates in lung and liver. Although organ-specific endothelial effects of LPS have been previously demonstrated [32,33] and may provide a rationale for isolated renal injury in our model, further experimental evidence is necessary to clarify this observation. Chronic kidney disease is an important risk factor for cardiovascular events and death in humans [34]. Therefore, future studies may use our model to address whether severe chronic renal injury in our model is capable of inducing damage and fibrosis in other organs over a longer time course.

CXCR4 is expressed by many cells including bone marrow-derived stem cells, leukocytes including neutrophils, macrophages and T cells and has multiple cell- and context-dependent effects [35]. Previously, ectopic overexpression of CXCR4 in podocytes due to loss of the *VHL* gene in intrinsic glomerular cells was shown to induce crescentic glomerulonephritis, which was attenuated by CXCR4 inhibition [17]. CXCR4 expression was also demonstrated in podocytes in renal specimens from patients with hypertensive nephropathy [36]. In another report, increased podocyte CXCR4 expression and oxidative stress was observed in murine adriamycin-induced nephropathy, where AMD3100 attenuated oxidative stress, podocyte injury and fibrosis [37]. We report elevated expression of CXCR4 mRNA and increased protein expression in and around glomeruli of AAV model mice, in addition to increased mRNA of the respective ligand CXCL12. Inhibition of CXCR4 with the FDA approved inhibitor AMD3100 increased the frequency of glomeruli exhibiting both crescents and fibrin extravasate together, which may suggest prolonged presence or reduced clearance of fibrin deposits in injured glomeruli. Based on unbiased MS-based proteomic and specific mRNA expression and immunolabeling analyses, we determined that CXCR4 inhibition attenuated leukocyte activation but not renal tissue infiltration. Presently, we cannot conclude if this effect of AMD3100 is systemic immunomodulation or local attenuation of renal inflammation. Future work may address the underlying mechanisms and more fully characterize the effect on disease phenotype and long-term scarring. Altogether, these studies encourage further investigation of CXCR4 as a potential target, for which we also provide evidence in our AAV model.

Besides CXCR4 inhibition, our model can help to investigate other novel candidates for therapeutic approach. For example, IL6 and TNF response signatures were up-regulated in our AAV model, therefore, upstream regulators such TLR4 that have been implicated in AAV [38] may present pharmacological targeting opportunities to be investigated in more detail in future studies. In two controlled trials, TNF inhibition had no advantage over conventional therapy; however, several case studies report positive response of patients that were refractory to conventional treatment [39]. More pre-clinical and clinical studies are

needed to fully evaluate the potential benefit of such alternative treatment approaches.

In summary, we have generated a robust, anti-MPO dependent murine model that exhibits clinical and histopathological changes consistent with those seen in human AAV. We observe acute injury and progression to scarring, comprising a highly inflammatory renal environment with substantial changes in matrisome expression. Our MS-based proteomic analysis provides a resource to aid in screening for potential drug targets that could improve currently approved treatments (**Figure 9**).

Material and methods

Study approval

Mostly female C57Bl6J littermates (8 -10 weeks of age) were maintained in a specific pathogen-free animal facility and controlled for good health and welfare (including posture and activity) daily. Handling of mice and experimental procedures were performed according to the French law for the protection of laboratory animals. Procedures were approved by the regional ethical committee for animal experimentation (CREMEAS) of the Strasbourg University, under the authorization number 17638-2017080312395908.

Acute and late-stage AAV mouse model protocol and AMD3100 treatment

Experimental groups consisted of at least 4 mice per time point and condition. The experiments of the AAV group were repeated at least twice independently. To induce AAV, female C57Bl6J mice (bred in house) were administered 100 μl sheep anti-rat glomerular basement membrane (αGBM) serum (Probetex, PTX-001S) via tail vein (i.v.) at day 0. Cross-reactivity with murine GBM epitopes was confirmed by indirect immunofluorescence using anti-GBM serum as primary antibody and detection using anti-sheep IgG, followed by streptavidin-Alexa488 conjugate (data not shown). At day 5, mice were administered 0.75 mg of murine monoclonal anti-MPO (αMPO) antibody clones 6D1 (Euromedex, BX-6D1-50MG and BX-6G4-50MG) and 100 μl LPS (Sigma, L6636-25MG) (0.5 μg/g) one hour later. Mouse monoclonal antibodies 6D1 (IgG2b) and 6G4 (IgG2c) directed against murine myeloperoxidase (MPO) were generated as described for anti-MPO antibody clone 8F4 [40]. Bulk (50 mg each) production of 6D1 and 6G4 was performed by BioXcell with permission of P. Heeringa. As controls, αGBM, αMPO and LPS were injected alone or in different pairwise combinations (αGBM/αMPO, αGBM/LPS, αMPO/LPS). As control for αGBM, mice were 100 μl PBS i.v. administered on day 0. As control for αMPO, mice were i.p. administered 0.75 mg each of isotype IgG2a and IgG2b (Euromedex, BE0086-50MG and BE0085-50MG), at day 5. As control for LPS, mice received 100 μl PBS i.p. one hour after αMPO or isotype control injections. Mice were sacrificed at days 12, 19, 24 and 29 under deep anesthesia (Ketamine/Xylazine i.p.) by transcardiac perfusion-fixation with 20 ml of PBS followed by 20 ml of 4% PFA. Renal tissue was snap frozen in liquid nitrogen and stored at -80°C for subsequent qPCR analysis, frozen in OCT for immunofluorescence analysis, and fixed overnight in 4% PFA for FFPE processing and immunohistochemistry. Mice in the AAV protocol (anti-GBM/anti-MPO/LPS) received daily injections of AMD3100 (Sigma, A5602) at 10 mg/kg daily or PBS in the control group for 12d starting at day 0.

Hematuria, proteinuria and body weight measurement

From day 0 to day 12 urine samples were collected to determine hematuria and proteinuria using Multistix 8 SG reagent strips (Siemens, 2164) according to manufacturer's instructions. Mice were manually restrained by gently clasping the scruff of the neck and the tail. To provoke miction, the lower abdomen was gently stimulated with a finger. According to the manufacturer, dipstick scores are quantitated as follows: hematuria; 0 = $<$10 Ery/μL, 0-1 = 25 Ery/μL, 1 = 80 Ery/μL, 1.5 $>$ 200 Ery/μL. Proteinuria; 1 = 30 mg/dl, 2 = 100 mg/dl, 3 = 300 mg/dl, 4 = 2000 mg/dL.

RNA extraction, reverse transcription and quantitative PCR (qPCR)

Frozen kidneys were processed in a tissue homogenizer (OMNI International Tissue MASTER 125) with 1 ml TRIZOL (Invitrogen, 12044977) for total RNA extraction according to manufacturers' instructions. Total RNA quantity and the purity was determined using a spectrometer (Nanodrop1000, Thermo Scientific). cDNA was prepared from 1 μg RNA after Desoxyribonuclease I treatment (0.5 U/μg RNA; Roche), followed by reverse transcription in RT buffer (Roche, 04716728001), primers (listed in **Supplementary Table S1**), dNTPs (4 mM final, Applied Biosystems, 4367381number) and MultiScribe reverse transcriptase (2.5 U/μl) (Applied Biosystems, 4308228). QPCR was performed using a QuantStudio 3 Real-Time qPCR System (Applied Biosystems, A28132). Reactions were performed in technical duplicates using a Sybr Green Master mix (ThermoFisher Scientific, 4344463) or Fast Taqman mix (ThermoFisher Scientific, 4444557). Measurements were normalized to murine GAPDH (Life Technology, 433764T) was using the comparative

cycle threshold method. Gene specific primer sequences are listed in **Supplementary Table S1**.

Immunofluorescence staining

Tissue sections (4 μm) kidneys embedded in OCT (Optimal cutting temperature compound, Sakura Finetek, number) were prepared with a cryostat microtome (LEICA CM3050S) and deposited on microscope slides (WVR, 631-0108). Tissue sections were rehydrated with PBS, permeabilized with PBS/Triton 0.25% (Merck, T8787) and washed 3 times with PBS. Tissues were incubated at RT for 1 hour with 5% normal donkey serum (NDS, Jackson ImmunoResearch) to block unspecific interactions, followed by incubation with primary antibodies O/N at 4°C. Slides were washed 3 times with PBS and incubated with secondary antibody diluted in 5% NDS/PBS and washed 3 times with PBS. Nuclei were stained using 4',6-Diamidine-2'-phenylindole dihydrochloride (DAPI) (Sigma) at 1:30,000 dilution for 10 minutes and washed 3 times with PBS. Coverslips were applied using a fluorescence conserving medium (Fluoromount G, Invℓtrogen, 00-4958-02).

Representative images of the fluorescent signals were acquired using an Axio Imager Z2 Fluorescent Microscope (Zeiss, 430000-9902) at 20X magnification using identical settings (e.g. microscope, magnification, light intensity, exposure time) for all images to be compared. Primary and secondary antibodies are listed in **Supplementary Table S2**.

LC-MS/MS sample preparation and measurements

Deparaffinized FFPE tissue sections were macrodissected to obtain 1−2 mm^3 tissue per sample and transferred into lysis buffer (4% SDS, 0.1M HEPES, pH 8). Proteins were extracted using Bioruptor ultrasonication (Diagenode, B01020001) (20 cycles, 40/20 sec ON/OFF, 4°C), heat induced antigen retrieval (2 h, 95°C), followed by an additional ultrasonication (10 cycles, 40/20 sec ON/OFF, 4°C). Samples were precipitated and the supernatant was incubated with 5 mM Tris(2-carboxyethyl) phosphine (TCEP) (Sigma Aldrich, 102372121) and 20 mM chloroacetamide (CAA) (Sigma Aldrich, 1002535380) for 30 min at RT in the dark. Protein concentration was determined using the bicinchoninic acid (BCA) assay (Thermo Scientific, 23225). Reduced and alkylated proteins were digested using SpeedBeads Magnetic Carboxylate (Cytiva, GE65152105050250, GE45152105050250) as published [41]. Then, 500 μg pre-washed 1:1 mixture of hydrophobic and hydrophilic beads were added to each sample and acetonitrile was added to a final concentration of 55% (v/v) at RT for 10 min followed by washing (2 × 70% ethanol, 1 × 100% acetonitrile) and drying for 5 min without heating (Eppendorf concentrator 5301). Dried beads were resuspended in 100 μL ammonium bicarbonate buffer (100 mM, pH 8) and Lys-C (Serva, 920987.01) was added at a 1:100 (wt/wt) ratio and incubated at 42°C for 2 h. Trypsin (Serva, 37286.03) digestion was done at a 1:25 (wt/wt) ratio of protease to protein overnight at 37°C. All samples were desalted using iST columns (PreOmics, PO00013) according to the manufacturer's protocol. Peptide concentration was determined using the BCA assay and 2 μg of each sample were further processed by addition of 11 iRT peptides (200 fmol/μL), Biognosys, Ki-3002-2), dried and stored at -80°C until LC-MS/MS measurement.

For LC-MS/MS measurements, each sample was reconstituted in 12 μL 0.1% formic acid (buffer A) and separated using an EASY-nLC™ 1000 UHPLC system (Thermo Fisher Scientific, LC120) at a flow rate of 350 nL/min. The column setup consisted of a μPac Trapping column (PharmaFluidics, 55250200018001) and a 200 cm μPac GEN1 analytical column (PharmaFluidics, 55250315018210) coupled to a Nanospray Flex™ ion source (Thermo Scientific, ES071) and a fused silica emitter (MS Wil, TIP1002005-5). For peptide separation, a 70 min linear gradient was used with increasing buffer B (80 % acetonitrile, 0.1 % formic acid) ranging from 8% to 40% buffer B, a 10 min linear gradient from 40% to 55% buffer B followed by 40 min 100% buffer B. Peptides were analyzed using a Q-Exactive Plus mass spectrometer (Thermo Scientific, San Jose, CA, IQLAAEGAAPFALGMBDK) operating in data independent acquisition (DIA) mode. For gas phase fractionation (GPF) library generation, a mastermix of all samples was injected six times and measured in DIA mode, each with a scan range of 100 *m/z*, covering in total a scan range of 400−1000 *m/z*. Survey scans were performed at 70k resolution, an automatic gain control (AGC) target of 1e6 and a maximum injection time (IT) of 80 ms followed by the fragment ion scans at 17.5k resolution with 4 *m/z* isolation window. For DIA of the actual samples, survey scans were performed at 70k resolution, an AGC target of 3e6 and a maximum injection time (IT) of 50 ms. For MS2 scans, peptides were fragmented using HCD and stepped collision energy 25, 30 and measured at 17.5k resolution with 24 *m/z* isolation window.

Tryptic, GPF refined spectral library generation by DIA-NN

Raw data were analyzed using DIA-NN (1.7.12) and a mouse proteome database (downloaded from ebi.ac.uk/reference_proteomes/ on 28th July 2021 (reference UP000000589 100909) containing 22001 entries. Sequences of common contaminants and 11 iRT peptides were manually appended. With the proteome FASTA file, a spectral library was

predicted using the default parameters in DIA-NN. The GPF dia files were then used to generate a GPF refined library. Precursors were restricted to 300 m/z to 1800 m/z, fragments were restricted to 200 m/z to 1800 m/z and retention time (RT) profiling was activated. Sample dia files were analyzed using DIA-NN with the refined library and default parameters [42].

Protein expression analysis

Differential abundance of proteins was performed using R [43] v4.1.0 in R Studio v1.4.1717 and the *limma* [44] package, using a predefined significance threshold of $p < 0.05$. Gene Ontology (GO) term enrichment (GO_Biological process_2018) was performed using the *Enrichr* tool (Ma'ayan laboratory) [45]. Significant deregulated protein expression analysis was performed by using the PANTHER version 11. Gene set enrichment analysis was performed by using WEB-based GEne SeT AnaLysis Toolkit (WebGestalt) based on the Gene Ontology functional database. The DIA spectral data, together with spectral libraries, search results and R scripts for data processing were made publicly available via the MASSIVE repository and can be accessed using the following repository identifiers: Massive: MSV000088028; ProteomeXchange: PXD028173. http://massive.ucsd.edu/ProteoSAFe/QueryPXD?id=PXD028173.

Microarray data analysis

Gene expression microarray datasets were downloaded from NCBI gene expression omnibus (GEO; GSE104948, GSE104954, glomerular and tubulointerstitial transcriptomes from European Renal cDNA Bank subjects and living donors) as raw data and processed using R [43] v4.0.2 in R studio v1.3.959. Data were normalized with the package *affy* [46] using the RMA method and a custom chip description file (BrainArray v25). Pathway analysis was performed using the Pathifier [47] implementation for R. Differential gene expression analysis was performed using the package *limma* [44] using Benjamini-Hochberg correction for multiple testing ($p < 0.05$). Matrix-associated genes were curated from annotations in PANTHER Database (ECM compartment) and Gene Ontology Functional Database (cellular components: collagen-containing ECM, collagen trimer). Graphs were plotted using *ggplot2* [48] and *ComplexHeatmap* [49] packages. Differentially expressed genes (vs. LD) were compared between AAV, FSGS and DN by associating the gene name with the directionality of differential expression and determining intersection and differences of genes with significant differential expression with a specific directionality. Human gene homologues of murine proteins were obtained using NCBI homologene. Concordant gene expression between human genes and human gene homologues of murine proteins was performed as described above.

AAV patient biopsies

Renal biopsies of AAV patients and healthy kidney donors were de-archived with approval of the ethics committee of the Medical University of Vienna (EK 1476/2017).

Histology and immunohistochemistry (IHC)

Formalin-fixed tissues were processed using an automated tissue processor (Tissue-Tek VIP, Sakura Finetek). Tissues were embedded in paraffin and 2μm sections were prepared for AFOG (acid fuchsine, orange G), sirius red (picric acid/direct red 80) and IHC.

AFOG staining was performed as follows: deparaffinization, Bouin's fixative (one hour), destaining in 80% EtOH (10 min), tap water wash (10 min); hematoxylin (Weigert) (5 min); tap water wash (10 min), phosphomolybdic acid staining (5 min), brief distilled water wash, AFOG solution staining (20 min), brief distilled water wash, dehydration and mounting with coverslip.

Sirius red staining was performed using a commercial kit (Morphisto 13425.00250) according to manufacturer's instructions. IHC was performed using specified antibodies (**Supplementary Table S3**).

Human IHC was performed on a Ventana Benchmark Ultra stainer (Ventana Medical Systems) except for Collagen III (manual). Murine IHC was performed manually. In brief, slides were deparaffinized, rehydrated and subjected to heat- or protease-induced antigen retrieval as specified in **Supplementary Table S3**. Endogenous peroxidases were blocked with 3% hydrogen peroxide in methanol for 10 minutes at RT. Protein blocking and primary antibody incubation was performed in 2% normal goat serum. Immunolabeling was amplified using polymer-based reagents for rabbit primary antibodies (Vector Laboratories, MP-7451) or avidin-biotin complex-based reagents for rat primary antibodies (Vector Laboratories, SP-2001, Amersham Biosciences, RPN1005V, Vector Laboratories, PK-6100) and developed using DAB substrate (Thermo Scientific, 34002) according to manufacturers' instructions. Counterstaining was performed using Mayer's Hematoxylin for 30 seconds, followed by dehydration and mounting with coverslip.

Whole slide imaging and software-assisted analysis of fibrosis (sirius red) and leukocytes (IHC)

Slides were imaged using a Pannoramic Flash II slide scanner (3DHistech), using 20x (mouse) or 40x (human) objectives and 2x doubling lens.

Quantification of staining signals was performed by a resident pathologist (AO) using QuPath [50]. In brief, stain vectors were estimated using the built-in color deconvolution functions before manual annotation of renal cortex using the polygon annotation tool. IHC and sirius red stains were quantitated using the built-in "positive cell detection" and "pixel classification" functions.

Morphological analysis of murine lesions

At least one hundred consecutive glomeruli were evaluated within one 2μm AFOG-stained section per mouse by a resident pathologist (AO) for presence of lesions as follows: presence of fibrinoid necrosis, crescent (extracapillary proliferation), or scarring (segmental or global sclerosis). Unless specifically stated, all glomeruli with crescents were counted as "crescents" (i.e. including crescents and necrosis), while all glomeruli with scars were counted as "scars" (i.e. including scars, crescents and necrosis).

Statistical analysis

GraphPad Prism software (version 8) was used for statistical analyses and graphical representations of data unless otherwise specified. For all data, normal distribution was assessed using the Shapiro-Wilk normality test. Data with a normal distribution were tested with an unpaired t-test or one-way ANOVA. Other data were tested using a Mann-Whitney test or non-parametric ANOVA. Symbols represent individual mice, horizontal lines and bars correspond to mean +/- SEM; * $p< 0.05$, ** $p < 0.01$, *** $p < 0.001$, **** $p < 0.0001$.

Funding was provided by ANR-PRCI, INSERM (GO) and FWF (RK). OS acknowledges funding by the Deutsche Forschungsgemeinschaft (DFG, SCHI 871/17-1, NY 90/6-1, SCHI 871/15-1, GR 4553/5-1, PA 2807/3-1, project-ID 431984000 – SFB 1453, project-ID 441891347 – SFB 1479, project-ID 423813989 – GRK 2606, project-ID 322977937 – GRK 2344), the ERA PerMed programme (BMBF, 01KU1916, 01KU1915A), the German-Israel Foundation (grant no. 1444), and the German Consortium for Translational Cancer Research (project ImproRec).

Author contribution

RK and GO conceptualized the study. CAF, AO, TF, MC, and TL performed experiments, analyzed and interpreted the data. AO performed IHC staining of human AAV tissues and analyzed the human Affymetrix data. CAF performed all mouse experiments and performed mRNA and immunofluorescence analysis of the kidneys. AO performed histopathological analysis of murine renal injury, performed IHC of murine tissues and quantified renal leukocytes. TF and MC performed the proteomics analysis. OS and MC supervised the proteomics analysis. TL generated the heatmaps for proteomics analysis. FS, HS and BL provided technical assistance. PH lab generated the MPO antibodies. CAF and AO wrote the manuscript, RK, GO and AR edited the manuscript. GO and RK supervised the study. All authors read and discussed the manuscript.

Declaration of competing interests

The authors declare no competing financial interests.

Acknowledgements

We acknowledge personnel from INSERM U1109, M. van der Heyden, A. Klein, C. A. Mariotte, A. De Cauwer and the personnel of the animal facility. We acknowledge Raul A. Mejia Pedroza for advice on pathway analysis, Margit Schmeidl for technical assistance, and Richard Kitching for helpful discussions.

Supplementary materials

Supplementary material associated with this article can be found in the online version at doi:10.1016/j.matbio.2022.01.001.

Received 31 August 2021;
Received in revised form 18 December 2021;
Accepted 5 January 2022
Available online 13 January 2022

Keywords:
Anti-neutrophil cytoplasmic antibody associated vasculitis;
AAV;
matrisome;
CXCR4

Abbreviations:
AGC, automatic gain control; αSMA, smooth muscle alpha-actin; AU, arbitrary unit; CFA, complete Freund's adjuvant; Col, collagen; CXCL1/2/12, chemokine (C-X-C motif) ligand 1/2/12; CXCR4, C-X-C motif chemokine receptor 4; DIA, data independent acquisition; DN, diabetic nephropathy; FN, fibronectin; FNGN, focal necrotizing glomerulonephritis; FoxP3, forkhead box P3; FSGS, focal segmental glomerulosclerosis; GBM, glomerular basement membrane; GPF, gas phase fractionation; ICAM1, intercellular Adhesion Molecule 1; IHC, indirect immunohistochemistry; IIF, indirect immunofluorescence; IL1β, interleukin 1 beta; IL6, interleukin 6; LC-MS/MS,

Liquid Chromatography with tandem mass spectrometry; LD, living donor; LPS, lipopolysaccharide; MCD, minimal change disease; mIgG, murine IgG; MMP9, matrix metallopeptidase 9; MPO, Myeloperoxidase; NE, neutrophil elastase; PCA, principal component analysis; PDS, pathway dysregulation scores; TGFβ, transforming growth factor beta; TNC, tenascin-C; VCAM1, vascular cell adhesion molecule 1; VCAN, versican

References

[1] A.R. Kitching, et al., ANCA-associated vasculitis, Nat. Rev. Dis. Primers 6 (2020) 1–27.

[2] A. Berti, D. Cornec, C.S. Crowson, U. Specks, E.L. Matteson, The Epidemiology of Antineutrophil Cytoplasmic Autoantibody-Associated Vasculitis in Olmsted County, Minnesota: A Twenty-Year US Population-Based Study, Arthritis Rheumatol. 69 (2017) 2338–2350.

[3] A.J. Mohammad, L.T.H. Jacobsson, A.D. Mahr, G. Sturfelt, M. Segelmark, Prevalence of Wegener's granulomatosis, microscopic polyangiitis, polyarteritis nodosa and Churg-Strauss syndrome within a defined population in southern Sweden, Rheumatology (Oxford) 46 (2007) 1329–1337.

[4] J.A. Tan, et al., Mortality in ANCA-associated vasculitis: ameta-analysis of observational studies, Ann. Rheum. Dis. 76 (2017) 1566–1574.

[5] N. Basu, et al., The characterisation and determinants of quality of life in ANCA associated vasculitis, Ann. Rheum. Dis. 73 (2014) 207–211.

[6] K. Raimundo, A.M. Farr, G. Kim, G. Duna, Clinical and Economic Burden of Antineutrophil Cytoplasmic Antibody-associated Vasculitis in the United States, J. Rheumatol. 42 (2015) 2383–2391.

[7] J.C. Jennette, P.H. Nachman, ANCA Glomerulonephritis and Vasculitis, CJASN CJN (2017) .02500317, doi: 10.2215/CJN.02500317.

[8] H. Xiao, P. Hu, R.J. Falk, J.C. Jennette, Overview of the Pathogenesis of ANCA-Associated Vasculitis, Kidney Dis. 1 (2015) 205–215.

[9] C. Bonnans, J. Chou, Z. Werb, Remodelling the extracellular matrix in development and disease, Nat. Rev. Mol. Cell Biol. 15 (2014) 786–801.

[10] D. Zhou, Y. Liu, Renal fibrosis in 2015: Understanding the mechanisms of kidney fibrosis, Nat. Rev. Nephrol. (2015), doi: 10.1038/nrneph.2015.215.

[11] H. Xiao, et al., Antineutrophil cytoplasmic autoantibodies specific for myeloperoxidase cause glomerulonephritis and vasculitis in mice, J. Clin. Invest. 110 (2002) 955–963.

[12] A.-J. Ruth, et al., Anti-Neutrophil Cytoplasmic Antibodies and Effector CD4+ Cells Play Nonredundant Roles in Anti-Myeloperoxidase Crescentic Glomerulonephritis, JASN 17 (2006) 1940–1949.

[13] P.C. Grayson, et al., Metabolic pathways and immunometabolism in rare kidney diseases, Ann. Rheum. Dis. 77 (2018) 1226–1233.

[14] M.E. Blaauboer, et al., Novel combination of collagen dynamics analysis and transcriptional profiling reveals fibrosis-relevant genes and pathways, Matrix Biol. 32 (2013) 424–431.

[15] A. Naba, et al., The matrisome: in silico definition and in vivo characterization by proteomics of normal and tumor extracellular matrices, Mol. Cell. Proteomics 11 (2012) M111.014647.

[16] D. Huugen, et al., Aggravation of anti-myeloperoxidase antibody-induced glomerulonephritis by bacterial lipopolysaccharide: role of tumor necrosis factor-alpha, Am. J. Pathol. 167 (2005) 47–58.

[17] M. Ding, et al., Loss of the tumor suppressor Vhlh leads to upregulation of Cxcr4 and rapidly progressive glomerulonephritis in mice, Nat. Med. 12 (2006) 1081–1087.

[18] A. Yuan, Y. Lee, U. Choi, G. Moeckel, A. Karihaloo, Chemokine receptor Cxcr4 contributes to kidney fibrosis via multiple effectors, Am. J. Physiol. Renal. Physiol. 308 (2015) F459–F472.

[19] M. Metzemaekers, M. Gouwy, P. Proost, Neutrophil chemoattractant receptors in health and disease: double-edged swords, Cell. Mol. Immunol. 17 (2020) 433–450.

[20] L. Shochet, S. Holdsworth, A.R. Kitching, Animal Models of ANCA Associated Vasculitis, Front. Immunol. 11 (2020) 525.

[21] S. Klahr, Progression of chronic renal disease, Heart Dis. 3 (2001) 205–209.

[22] E. De Clercq, The AMD3100 story: the path to the discovery of a stem cell mobilizer (Mozobil), Biochem. Pharmacol. 77 (2009) 1655–1664.

[23] A Phase 3 Clinical Trial of CCX168 (Avacopan) in Patients With ANCA-Associated Vasculitis - Full Text View - ClinicalTrials.gov. https://clinicaltrials.gov/ct2/show/NCT02994927.

[24] L. Schaefer, Decoding fibrosis: Mechanisms and translational aspects, Matrix Biol. 68−69 (2018) 1–7.

[25] M. Allinovi, L. De Chiara, M.L. Angelotti, F. Becherucci, P. Romagnani, Anti-fibrotic treatments: A review of clinical evidence, Matrix Biol. 68−69 (2018) 333–354.

[26] A.R. Kitching, et al., The requirement for granulocyte-macrophage colony-stimulating factor and granulocyte colony-stimulating factor in leukocyte-mediated immune glomerular injury, J. Am. Soc. Nephrol. 13 (2002) 350–358.

[27] K.N. Konstantinov, C.J. Ulff-Møller, A.H. Tzamaloukas, Infections and antineutrophil cytoplasmic antibodies: triggering mechanisms, Autoimmun. Rev. 14 (2015) 201–203.

[28] I. Neumann, H. Regele, R. Kain, R. Birck, F.T Meisl, Glomerular immune deposits are associated with increased proteinuria in patients with ANCA-associated crescentic nephritis, Nephrol. Dial. Transplant. 18 (2003) 524–531.

[29] Y. Nozaki, New Insights Into Novel Therapeutic Targets in ANCA-Associated Vasculitis, Front. Immunol. 12 (2021) 1088.

[30] K. Midwood, et al., Tenascin-C is an endogenous activator of Toll-like receptor 4 that is essential for maintaining inflammation in arthritic joint disease, Nat. Med. 15 (2009) 774–780.

[31] J. Ishizaki, et al., Targeted proteomics reveals promising biomarkers of disease activity and organ involvement in antineutrophil cytoplasmic antibody-associated vasculitis, Arthritis Res. Ther. 19 (2017) 218.

[32] A. Aslan, et al., Organ-Specific Differences in Endothelial Permeability-Regulating Molecular Responses in Mouse and Human Sepsis, Shock 48 (2017) 69–77.

[33] A. Jambusaria, et al., Endothelial heterogeneity across distinct vascular beds during homeostasis and inflammation, eLife 9 (2020) e51413.

[34] A.S. Go, G.M. Chertow, D. Fan, C.E. McCulloch, C. Hsu, Chronic Kidney Disease and the Risks of Death, Cardiovascular Events, and Hospitalization, N. Engl. J. Med. 351 (2004) 1296–1305.

[35] J.F. Wang, Z.Y. Liu, J.E. Groopman, The alpha-chemokine receptor CXCR4 is expressed on the megakaryocytic lineage from progenitor to platelets and modulates migration and adhesion, Blood 92 (1998) 756–764.

[36] M.A. Neusser, et al., Human Nephrosclerosis Triggers a Hypoxia-Related Glomerulopathy, Am. J. Pathol. 176 (2010) 594–607.
[37] H. Mo, et al., C-X-C Chemokine Receptor Type 4 Plays a Crucial Role in Mediating Oxidative Stress-Induced Podocyte Injury, Antioxid. Redox. Signal. 27 (2017) 345–362.
[38] K.M. O'Sullivan, S.L. Ford, A. Longano, A.R. Kitching, S.R. Holdsworth, Intrarenal Toll-like receptor 4 and Toll-like receptor 2 expression correlates with injury in antineutrophil cytoplasmic antibody-associated vasculitis, Am. J. Physiol. Renal. Physiol. 315 (2018) F1283–F1294.
[39] S.P. McAdoo, C.D. Pusey, Is there a role for TNFα blockade in ANCA-associated vasculitis and glomerulonephritis? Nephrol. Dial. Transplant. 32 (2017) i80–i88.
[40] M. van Leeuwen, et al., Accumulation of myeloperoxidase-positive neutrophils in atherosclerotic lesions in LDLR-/- mice, Arterioscler. Thromb. Vasc. Biol. 28 (2008) 84–89.
[41] C.S. Hughes, et al., Single-pot, solid-phase-enhanced sample preparation for proteomics experiments, Nat. Protoc. 14 (2019) 68–85.
[42] V. Demichev, C.B. Messner, S.I. Vernardis, K.S. Lilley, M. Ralser, DIA-NN: neural networks and interference correction enable deep proteome coverage in high throughput, Nat. Methods 17 (2020) 41–44.
[43] R Core Team, R: A Language and Environment for Statistical Computing, R Foundation for Statistical Computing, 2020.
[44] M.E. Ritchie, et al., limma powers differential expression analyses for RNA-sequencing and microarray studies, Nucleic Acids Res. 43 (2015) e47.
[45] M.V. Kuleshov, et al., Enrichr: a comprehensive gene set enrichment analysis web server 2016 update, Nucleic. Acids. Res. 44 (2016) W90–W97.
[46] L. Gautier, L. Cope, B.M. Bolstad, R.A. Irizarry, affy—analysis of Affymetrix GeneChip data at the probe level, Bioinformatics 20 (2004) 307–315.
[47] Y. Drier, M. Sheffer, E. Domany, Pathway-based personalized analysis of cancer, PNAS 110 (2013) 6388–6393.
[48] H. Wickham, ggplot2: Elegant Graphics for Data Analysis, Springer-Verlag, New York, 2016.
[49] Z. Gu, R. Eils, M. Schlesner, Complex heatmaps reveal patterns and correlations in multidimensional genomic data, Bioinformatics (2016).
[50] P. Bankhead, et al., QuPath: Open source software for digital pathology image analysis, Sci. Rep. 7 (2017) 16878.